The Effect of a Plasma Sheath on Hypersonic Flight Communications

by

Hiroshi Taneda

S.B. Aeronautics, Tokyo University, 1981
S.M. Aeronautics, Tokyo University, 1983

SUBMITTED IN PARTIAL FULFILLMENT OF THE
REQUIREMENTS FOR THE DEGREE OF

Master of Science
in
Aeronautics and Astronautics
at the
Massachusetts Institute of Technology
May 1990

Signature of Author _____

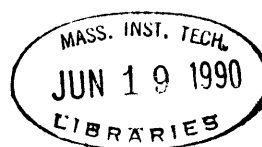Department of Aeronautics and Astronautics
May 1990

Certified by _____

Professor Daniel E. Hastings, Thesis Supervisor
Department of Aeronautics and Astronautics

Accepted by _____

Professor Harold Y. Wachman, Chairman
Department Graduate Committee

Aero

The Effect of a Plasma Sheath
on Hypersonic Flight
Communications
by
Hiroshi Taneda

Submitted to the Department of
Aeronautics and Astronautics
in partial fulfillment of the
requirements for the degree of
Master of Science in Aeronautics and Astronautics

The attenuation of electromagnetic waves propagating through a plasma sheath surrounding a sigle-stage-to-orbit vehicle with a scramjet was estimated. The forebody of the vehicle is simulated by a two dimensional wedge and the chemical composition and the effective dielectric coefficient in the high temperature air associated with the shock and the boundary layer over the wedge are calculated. The flow analysis includes the finite rate chemistry in the inviscid region and assumes chemical equilibrium in the boundary layer.

Three different typical trajectories are selected and the effects of velocity, wedge angle, and wall temperature on the attenuation are studied. The results show that the attenuation becomes significant above Mach 16 for radio frequencies below X band. The critical radio frequency decreases with increasing altitude. The increase in wedge angle above 10° increases the attenuation drastically while the effect of wall temperature is relatively small for the temperature range between 1000 K and 2000 K.

Acknowledgements

Contents

3

List of Figures

List of Tables

Chapter 1

Introduction

Inspired by the National Aero-Space Program, which started in 1985 in the United States, research on hypersonic flight has been actively pursued in various nations. This hypersonic research has been aimed mainly at the development of a reusable hypersonic vehicle with a supersonic combustion ramjet or SCRAMJET.

One of the most challenging concepts of this type of vehicle is the Single Stage To Orbit vehicle or SSTO vehicle which would take off horizontally and fly up to orbital speeds in the atmosphere. A transatmospheric air-breathing vehicle, which needs to provide sufficient air for the engine opperation, must be accelerated at relatively lower altitudes compared with the conventional rocket boosters. On the other hand, in order to avoid excessive dynamic pressure and aerodynamic heating for the structures and materials, higher altitudes are desirable.

Because of these constraints, the trajectory of the SSTO vehicle will be constrained into a very narrow region. An important question which should be taken into account for the trajectory is the interference between the electromagnetic waves used for communication and the plasma sheath around the vehicle.

A vehicle flying in the atmosphere at high velocities becomes surrounded by regions of ionized gas that affect the propagation of electromagnetic waves to and from the vehicle. The kinetic energy in a hypersonic free stream is converted to the internal energy of the gas across the strong bow shock wave, creating very high temperatures in the shock layer near the nose. If the temperature is high enough,

ionization is present and a large number of free electrons are produced throughout the shock layer.

Downstream of the nose region, a boundary layer grows along the surface of the vehicle. Since the Mach number at the outer edge of the boundary layer is still high, the intense frictional dissipation within the hypersonic boundary layer creates high temperatures and causes chemical reactions.

The ions and electrons produced in the high temperature air around the vehicle create a plasma sheath, which interacts with electrcmagnetic waves propagating to and from the vehicle. If the attenuation of the electromagnetic waves due to the plasma sheath is excessively high, then a communication blackout occurs.

The problem of communications blackout and the flow analysis related to this problem were extensively studied in the 1950s and 1960s mainly for reentry vehicles such as the Apollo[1,2,3]. Since a reentry vehicle usually has a blunt body, these studies mainly focused on the analysis of the inviscid ionized gas over a blunt nose. The SSTO vehicle, however, will have a slender body and the effect of a boundary layer is expected to be much more important. The trajectory at relatively low altitudes is also a clear difference from other reentry vehicles.

In order to evaluate the interference between the electromagnetic waves and the plasma sheath, it is necessary to estimate the flow properties around the vehicle. The accurate estimation of the flow around the actual configuration requires computations which solve the full 3-D Navier Stokes equations including a chemical model. However, these computations, which need an extremely large computation time even with the most advanced computers, are not adequate for the parametric study in the wide range of the flight conditions while the vehicle configuration is not well determined yet. Therefore this thesis only considers very simple configurations and focuses on the general effects of the altitude, velocity, shock angle and wall temperature.

Since the major chemical reactions are caused by the strong shock wave which is generated by the forebody, this thesis only considers the flow regions around the forebody. Although no specific configuration is determined yet, the typical concepts of the SSTO vehicle have a slender forebody with a small bluntness at the nose. In

this thesis, two-dimensional wedges with a relatively small vertex angle are examined as the forebody geometry. Actual vehicles,however, have always some finite bluntness at the nose and a large number of electrons may be produced at the stagnation region. Since this effect of stagnation region is not taken into account in the wedge model, the flow analysis is only valid at the location which is sufficiently downstream from the nose. By ignoring the finite bluntness, the flow model may underestimate the electron density near the nose.

The goals of this thesis is to estimate the degree of attenuation of electromagnetic waves propagating to and from the SSTO vehicle and to evaluate the effects of trajectory, velocity, wedge angle, and wall temperature. In chapter 2, the typical trajectories are selected to determine the flight conditions for the evaluation of the flow properties around the vehicle. Chapter 3 states the flow model and the approach to calculate the flow properties over a wedge, and chapter 4 describes the approach to evaluate the attenuation of electromagnetic waves propagating in that flow. The numerical results are presented and discussed in chapter 5 and the conclusions are stated in chapter 6.

Chapter 2

Trajectory

2.1   Trajectory Model

This chapter selects the typical trajectories of a SSTO vehicle to determine the flight conditions, which will be used for the evaluation of the flow properties around the vehicle.   The flight trajectory of a hypersonic vehicle with a SCRAMJET has several constraints as follows:

- Sufficient combustor inlet pressure, of the order of one atmosphere, is required.

- The dynamic pressure and aerodynamic heating must not be excessively large.

The dynamic pressure limitation is generally less severe than the heating limitation which depends on the cooling technique.   Because of these constraints, the flight envelope is constrained into a very narrow corridor.   In order to evaluate the typical trajectory of the vehicle, this chapter follows a simplified trajectory analysis presented in Ref. [4].

The assumptions in this analysis are as follows:

- Constant overall efficiency η_{ov}, which is the product of thermal efficiency(the ratio of mechanical work to thermal energy) and propulsive efficiency(the ratio of propulsive work to total mechanical work),that is, the ratio of propulsive

10

work to thermal energy. This efficiency is defined as

$$\eta_{ov} \equiv \frac{F u_0}{\dot{m}_f h} \tag{2.1}$$

where F is thrust, u_0 is flight velocity, $\dot{m}_f$ is fuel mass flow, and h is fuel heat value.

• Constant drag coefficient C_D.

• Constant fuel/air mass ratio f.

• Potential energy is negligible compared with kinetic energy.

The governing equations of motion of a vehicle flying at a velocity u_0 along a flight path inclined at the angle θ above the local horizontal, as shown in Fig. 2.1, are

$$F - D - mg \sin \theta = \frac{du_0}{dt} m \tag{2.2}$$

$$L + m \frac{u_0^2}{R_{earth}} = mg \tag{2.3}$$

where m is the mass of the vehicle, R_{earth} is the radius of the earth, and θ is assumed to be small.
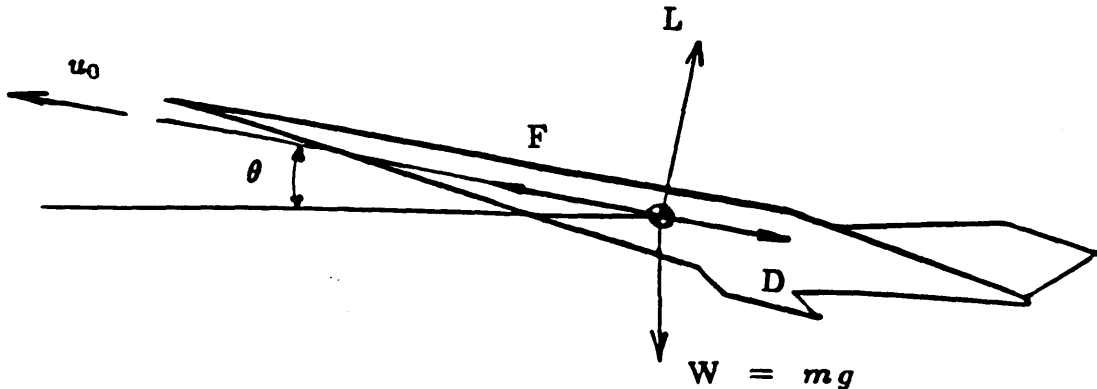
Figure 2.1: Force Diagram for Hypersonic Vehicle

Lift L and drag D are written as

$$L = \frac{1}{2}\rho u_0^2 A_W C_L \tag{2.4}$$

$$D = \frac{1}{2}\rho u_0^2 A_W C_D \tag{2.5}$$

where ρ is the air density, A_W is the wing area, C_L is the lift coefficient, and C_D is the drag coefficient.

Neglecting the $\sin\theta$ term, Eq.(2.2) can be written as

$$m\frac{d}{dt}(\frac{u_0^2}{2}) = Fu_0(1 - \frac{D}{F}) \tag{2.6}$$

From Eq. (2.1),

$$
\begin{aligned}
Fu_0 &= \eta_{ov}\dot{m}_f h \\
&= -\eta_{ov}h\frac{dm}{dt}
\end{aligned}
\tag{2.7}
$$

The fuel mass flow is related to the air capture area A_0 as

$$\dot{m}_f = f\rho u_0 A_0 \tag{2.8}$$

From equation (2.7) and (2.8),

$$\rho = \frac{F}{A_0\eta_{ov}f\,h} \tag{2.9}$$

Substituting Eqs. (2.5),(2.7), and (2.9) in Eq.(2.6),

$$mu_0 du_0 = -\eta_{ov}hdm(1 - \frac{A_W}{A_0}\frac{C_D}{\eta_{ov}f}\frac{u_0^2}{2h}) \tag{2.10}$$

Integrating this equation, we have

$$\frac{m}{m_0} = [1 - \frac{A_W}{A_0}\frac{C_D}{\eta_{ov}f}\frac{u_0^2}{2h}]^{\frac{A_0}{A_W}\frac{f}{C_D}} \tag{2.11}$$

The balance of the transverse force at the orbital velocity V_{orb} is

$$mg = m\frac{V_{orb}^2}{R_{earth}} \tag{2.12}$$

From Eq.(2.3) and Eq.(2.12), the air density is written as

$$\rho = \frac{2mg}{A_W C_L u_0^2}(1 - \frac{u_0^2}{V_{orb}^2}) \tag{2.13}$$

12

where m is given by Eq.(2.11)

Equation(2.13) gives the air density in terms of the vehicle velocity along a trajectory. In this work, *the U.S. Standard Atmosphere* [5] is used to obtain the corresponding altitude from the density so that the altitude-velocity relation of the trajectory can be determined.

The controlling parameter of the trajectory is *the modified wing loading*

$$\frac{m}{A_W C_L}$$

This parameter will be determined by the constraints mentioned in the first part of this chapter.

2.2 Typical Results

In this work, a low-earth orbit with the altitude of $200 Km$ is considered. The corresponding orbital velocity is about $7.8 Km/sec$.

Figure 2.2 shows the typical trajectories determined by Eq.(2.13) and Eq.(2.11) with $A_0/A_W = 0.3$, $\eta_{ov} = 0.6$, and $C_D = 0.02$. Three different values of modified wing loading are chosen to study the effect of the different trajectories on the communications later. Constant dynamic pressure lines are also shown in the same figure.

The scramjet is to be the dominant engine cycle, providing the thrust for acceleration from about Mach 5 to 20; however, since the scramjet relies on ram forces to compress the air, the vehicle must first be accelerated to the necessary speed for the scramjet operation by other engine cycles such as turbojets or ramjets. After the vehicle reaches about Mach 20, the dynamic pressure decreases rapidly as the vehicle ascends to the orbital altitude and the rocket will be turned on to provide the remaining acceleration to the orbit.

Current scramjet studies have mainly focused on the dynamic pressure range from 500 psf to 2000 psf or about 0.2 atm to 1 atm. The dynamic pressure along the middle trajectory in Fig.2.2 varies from 1.4 atm at V=1.5 Km/s(M=5) to 0.2 atm at V=6.7

Km/s(M=20). The dynamic pressure along the upper trajectory becomes less than 0.2 atm above V=5.3 Km/s(M=16) and that of the lower trajectory exceeds 2 atm below V=3.0 Km/s (M=10). Thus the upper and lower trajectories are selected as bounds.
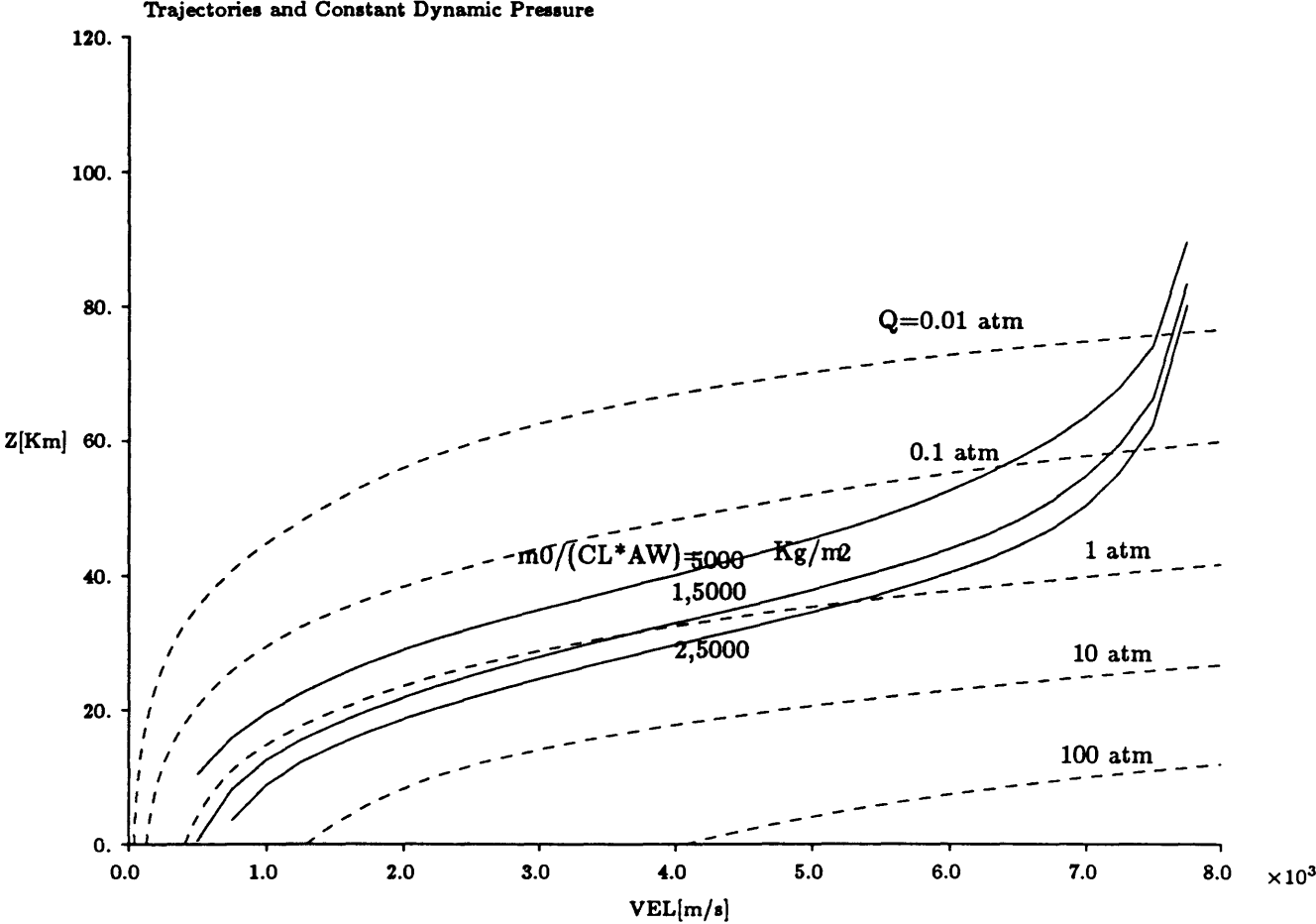
Figure 2.2: Typical Trajectories and Constant Dynamic Pressure

Chapter 3

Flow Model

This chapter develops a model for the analysis of the flow properties over a wedge, which is chosen as the simplified geometry of the forebody of a SSTO vehicle.

Since the main focus of the thesis is the attenuation of the electromagnetic waves propagating through a plasma sheath and the attenuation mainly depends on the electron density, the production of the electrons is the major interest. In order to estimate the electron density, a flow analysis including chemical reactions is required.

Figure 3.1 shows the schematic of the flow over a wedge, the upper surface of which is inclined at the angle of θ to the free stream. The flow behind the oblique shock wave consists of a boundary layer and an essensially inviscid region between the boundary layer and the shock.

Across the shock, the pressure and temperature are rapidly increased within the shock front, and the internal energy of the gas is redistributed in translation, rotation, vibration, dissociation, and ionization. The translational and rotational modes require a few molecular collisions to reach the local equilibrium and since the mean free path is small throughout the trajectories of interest, these modes are considered to be in equilibrium right behind the shock front.

The vibrational and chemical properties, however, require greater numbers of collisions to approach the new equilibrium properties. Thus, the relaxation times for these modes become important. Although there is a finite region where the vibrational mode is not in equilibrium, the relaxation length of the vibration is much

shorter than that of the dissociation and ionization along the trajectories of interest [6]. Therefore, in this work, it is assumed that the thermal equilibrium is always established immediately.

The first section of this chapter treats the inviscid flow region, where the chemical nonequilibrium is considered, and the second section treats the boundary layer.

3.1   Inviscid Chemically Nonequilibrium Flows

The shock wave generated over a straight wedge is curved due to the nonequilibrium process behind the shock. The shock angle tends to be the value of the frozen shock near the leading edge and far downstream, the shock angle approaches the equilibrium value as shown in Fig. 3.2.

The difference of the shock angle between the equilibrium and nonequilibrium flow is, however, very small for a small deflection angle θ throughout the trajectories of interest. Therefore it is assumed here that the shock is straight with the shock angle of the frozen shock. Corresponding to this assumption, the following assumptions are also made behind the shock:

- The pressure and velocity are constant.

- The velocity vector is parallel to the wall.

Figure 3.3 shows the simplified flow model with the above assumptions. Along each straight streamline, the flow is one dimensional.

3.1.1   Governing Equations

The governing equations of the flow are

- Global continuity

$$\frac{d(\rho u)}{dx} = 0 \tag{3.1}$$

- Species continuity

$$\frac{d(\rho_i u)}{dx} = \dot{w}_i \tag{3.2}$$

16

- **Momentum**

$$\rho u \frac{du}{dx} = -\frac{dp}{dx} \tag{3.3}$$

- **Energy**

$$\frac{d}{dx}\left(h + \frac{u^2}{2}\right) = 0 \tag{3.4}$$

- **Equation of state**

$$p = \rho R T \tag{3.5}$$

- **Enthalpy**

$$h = \sum_i c_i h_i \tag{3.6}$$

where ρ_i is the density of species i, that is, the mass of species i per unit volume of mixture. $\dot{w}$ is the local rate of change of ρ_i due to chemical reactions, which is written as

$$\dot{w}_i = M_i \frac{dn_i}{dt} \tag{3.7}$$

where M_i is the molecular weight of species i, that is, the mass of species i per mole of species i, n_i is the concentration of species i, h is the enthalpy of the mixture per unit mass and h_i is that of species i, and c_i is the mass fraction of species i, which is written as

$$c_i = \frac{\rho_i}{\rho} \tag{3.8}$$

R is the specific gas constant

$$R = \frac{\Re}{M} \tag{3.9}$$

$$M = \left(\sum_i \frac{c_i}{M_i}\right)^{-1} \tag{3.10}$$

17

where $\Re$ is the universal gas constant and M is the mixture molecular weight. Substituting Equations(3.7) and (3.8) in Eq.(3.2) and using Eq.(3.1)[1],

$$\rho u \frac{d\eta_i}{dx} = \frac{dn_i}{dt} \tag{3.11}$$

where η is the mole-mass ratio, or the number of moles of species i per unit mass

$$\eta_i = \frac{c_i}{M_i} \tag{3.12}$$

The momentum equation(3.3) is readily satisfied because of the assumptions.

$$\frac{du}{dx} = \frac{dp}{dx} = 0$$

The energy equation becomes

$$\frac{dh}{dx} = 0 \tag{3.13}$$

Using Eq.(3.12), Eq.(3.6) can be written as

$$0 = \sum_i \eta_i \frac{dH_i}{dx} + \sum_i H_i \frac{d\eta_i}{dx} \tag{3.14}$$

where H_i is the enthalpy per unit mole. Since H_i is a function of only T,

$$\frac{dT}{dx} = -\frac{\sum_i H_i \frac{d\eta_i}{dx}}{\sum_i \eta_i \frac{dH_i}{dT}} \tag{3.15}$$

Equations(3.11) and (3.15) can be integrated numerically. The reaction rate $\frac{dn_i}{dt}$ in Eq.(3.11) is obtained by the chemical rate equations.

3.1.2 Finite Rate Chemistry

The general elemental chemical reactions, each of which takes places in a single step, of a gas mixture of n species can be written as

$$\sum_{i=1}^{n} \nu'_{ir} A_i \rightleftharpoons \sum_{i=1}^{n} \nu''_{ir} A_i \tag{3.16}$$

---

[1]Since the number of unknowns is the number of species plus 2(ρ and T), all these unknowns are determined by Eqs.(3.2),(3.4), and (3.5) with Eq.(3.6). Thus, strictly speaking, Eq.(3.1) is an extra condition. However, for most cases considered here, Eq.(3.1) is essentially satisfied with only a few exceptions, where the density changes by the order of 10 %. In such cases, the assumption of straight shock gives a non-conservative mass flow behind the shock due to the variation of the density along the hypothetical straight stream lines.

where A_i represents the chemical species and $\nu_{ir}\prime$ and $\nu_{ir}\prime\prime$ represent the stoichiometric mole numbers of the reactants and products in the rth reaction, respectively.

The net reaction rate of the ith species is given by

$$\frac{dn_i}{dt} = (\nu_{ir}'' - \nu_{ir}')[k_f^r \prod_i n_i^{\nu_{ir}'} - k_b^r \prod_i n_i^{\nu_{ir}''}] \qquad (3.17)$$

where n_i is the concentration of the ith species and the k_f^r and k_b^r represent the forward and backward reaction rate constant in the rth reaction, respectively. k_f^r and k_b^r have a relation

$$\frac{k_f^r}{k_b^r} = K_c^r \qquad (3.18)$$

where

$$K_c^r = \prod_i n_i^{\nu_{ir}'' - \nu_{ir}'} \qquad (3.19)$$

is the equilibrium constant based on concentrations, which is related to the equilibrium constant K_p as

$$K_c^r = K_p^r(\frac{1}{\Re T})^{\sum_i \nu_{ir}'' - \nu_{ir}'} \qquad (3.20)$$

where $\Re$ is the universal gas constant and T is the temperature.

The kinetic mechanism and the values of the rate constants for high temperature air were compiled by Dunn and Kang in Ref.[14] and the table based on their work is shown in Ref.[7]. In this table, the forward rate constant is given by the following form

$$k_f^r = C_f^r T^{n_f^r} \exp\left(-E_f^r/kT\right) \qquad (3.21)$$

where k is the Boltzmann constant, E_f^r is the activation energy, and C_f^r and n_f^r are constants. Although the backward rate constants are obtained by Eq.(3.18), Dunn and Kang defined the backward rate coefficient directly in the form

$$k_b^r = C_b^r T^{n_b^r} \exp\left(-E_b^r/kT\right) \qquad (3.22)$$

The reaction mechanism and the parameters needed are shown in Table A.1 in Appendix A.

19

3.2 Boundary Layer

The mechanism of the transition of a boundary layer at hypersonic speeds is not well understood and the accurate prediction of transition is one of the leading questions in research in fluid mechanics.

Stetson [8] shows the transition Reynolds number Re_T, based on the flow properties at the edge of the boundary layer and the distance from the leading edge, for sharp cones in both wind tunnels and free flight. The results show the drastic increase of Re_T with the Mach number M_e at the edge of the boundary layer, especially above $M_e = 4$. According to these results, the transition point is more than 10 m downstream from the leading edge for $M_e \geq 12$ or $V \geq 4\,Km$ along the typical trajectories[4].

Assuming that there is not a significant difference in Re_T between a cone and wedge, the boundary layer on the wedge-shaped forebody, the length of which is the order of 10 m, is expected to be fully laminar for $M_e \geq 12$. Since the communication problem due to a plasma is expected to be serious only at high Mach numbers through the trajectories, the boundary layer is assumed to be fully laminar in this work. For simplicity, it is also assumed that the chemically reacting boundary layer is in equilibrium; with this assumption, the velocity and enthalpy have self-similar solutions.

3.2.1 Self-similar Solutions

Since the equilibrium chemical composition in the boundary layer is determined by the pressure and enthalpy of the gas mixture, the enthalpy profile needs to be determined to obtain the species concentrations while the pressure is considered to be constant across the boundary layer.

Although the main interest is the electron density, the major species in the boundary layer are diatomic molecules such as N_2, O_2, and NO and atoms such as O and N unless the temperature exceeds 9000 K[9], which is sufficiently higher than the expected maximum temperature throughout the trajectories. The concentrations of

for most cases considered here.

Therefore the contribution of the diffusion of ions and electrons to the energy equation of the mixture is negligible. In the diffusion mechanism, nitrogen and oxygen behave similarly and the distinction between them is not important compared with that between diatomic molecules and atoms. Hence the chemical composition of the mixture can be approximately grouped into two species:one contains diatomic molecules and the other contains atoms.

With this binary gas assumption, the boundary layer equations become:

- Global continuity

$$\frac{\partial(\rho u)}{\partial x} + \frac{\partial(\rho v)}{\partial y} = 0 \qquad (3.23)$$

- Species continuity

$$\rho u \frac{\partial c_i}{\partial x} + \rho v \frac{\partial c_i}{\partial y} = \frac{\partial}{\partial y}(\rho D_{12}\frac{\partial c_i}{\partial y}) + \dot{w}_i \qquad (3.24)$$

- x momentum

$$\rho u \frac{\partial u}{\partial x} + \rho v \frac{\partial u}{\partial y} = -\frac{\partial p}{\partial x} + \frac{\partial}{\partial y}(\mu\frac{\partial u}{\partial y}) \qquad (3.25)$$

- y momentum

$$\frac{\partial p}{\partial y} = 0 \qquad (3.26)$$

- Energy

$$\rho u \frac{\partial h_0}{\partial x} + \rho v \frac{\partial h_0}{\partial y} = \frac{\partial}{\partial y}\left[\frac{\mu}{P_r}\frac{\partial h_0}{\partial y} + \mu(1-\frac{1}{P_r})\frac{1}{2}\frac{\partial u^2}{\partial y}\right] - \frac{\partial}{\partial y}\left[(\frac{1}{L}-1)\rho D_{12}\sum_i h_i\frac{\partial c_i}{\partial y}\right]$$

$$(3.27)$$

where D_{12} is the diffusion coefficient between species 1 and 2, and P_r and L are Prandtl number and Lewis number, respectively

$$P_r = \frac{\mu c_{pf}}{k}$$

$$L = \frac{\rho D_{12} c_{pf}}{k} \qquad (3.28)$$

and c_{pf} is the frozen specific heat

$$c_{pf} = \sum_i c_i c_{pi}$$

$$c_{pi} = \frac{dh_i}{dT} \tag{3.29}$$

The boundary layer equations (3.23)-(3.27) are reduced to ordinary differential equations for some special cases by Lees-Dorodnitsyn transformation. The transformation for two dimensional flow are

$$\xi = \int_0^x \rho_e \mu_e u_e \, dx \tag{3.30}$$

$$\eta = \frac{\rho_e u_e}{(2\xi)^{\frac{1}{2}}} \int_0^y \frac{\rho}{\rho_e} \, dy \tag{3.31}$$

First, $u(\xi, \eta), c_i(\xi, \eta)$, and $h_0(\xi, \eta)$ are assumed to have similar solutions as

$$f'(\eta) = \frac{u}{u_e} \tag{3.32}$$

$$g(\eta) = \frac{h_0}{h_{0e}} \tag{3.33}$$

$$z_i(\eta) = \frac{c_i}{c_{ie}} \tag{3.34}$$

where the suffix e denotes the value at the outer edge of the boundary layer. Then the equations (3.23)-(3.27) become(see Ref[10])

$$\left(\frac{C}{S} z_i'\right)' + f z_i' = \frac{2\xi f' z_i}{c_{ie}} \frac{dc_{ie}}{d\xi} - \frac{2\xi \dot{w}_i}{\rho \rho_e u_e^2 \mu_e c_{ie}} \tag{3.35}$$

$$(Cf'')' + ff'' = \frac{2\xi}{u_e} \frac{du_e}{d\xi} \left[(f')^2 - \frac{\rho_e}{\rho} \right] \tag{3.36}$$

$$\left(\frac{C}{P_r} g'\right)' + f g' = \frac{2\xi f' g}{h_{0e}} \frac{dh_{0e}}{d\xi} + \left[\frac{C}{S} \left(\frac{1}{L} - 1\right) \sum_i \frac{h_i c_{ie}}{h_{oe}} z_i' \right]'$$

$$+ \frac{u_e^2}{h_{0e}} \left[\left(\frac{1}{P_r} - 1\right) C f' f'' \right]' \tag{3.37}$$

where the prime denotes the partial derivative with respect to η, S is the Schmidt number

$$S = \frac{\mu}{\rho D_{12}} \tag{3.38}$$

and C denotes the "rho-mu" ratio

$$C = \frac{\rho \mu}{\rho_e \mu_e} \tag{3.39}$$

22

From the assumptions made in the previous section,

$$\frac{du_e}{d\xi} = \frac{dh_0}{d\xi} = 0 \tag{3.40}$$

Then Equations(3.36) and (3.37) do not depend on ξ; $u(\xi, \eta)$ and h_0 have similar solutions, as shown in Eq.(3.32) and (3.33). On the other hand, $c_i(\xi, \eta)$ has a similar solution only if the c_{i_e} and $\dot{w}$ terms are constant; a special case is the frozen flow when $\dot{w}$ is zero. Equations(3.36) and (3.37) can be significantly simplified by assuming that the Prandtl number and Lewis nunmber are both unity. In this case, Eq.(3.36) and (3.37) become

$$(Cf'')' + ff'' = 0 \tag{3.41}$$

$$(Cg')' + fg' = 0 \tag{3.42}$$

The boundary conditions are

- At the wall

$$f = f' = 0, \qquad\qquad g = g_w (fixed\ wall\ temperature)^2 \tag{3.43}$$

- At the boundary layer edge $\eta \to \infty$

$$f' = 1, g = 1 \tag{3.44}$$

f' and g satisfy the same ordinary differential equations and the Crocco's integral is obtained using the boundary conditions for f and g

$$g = g_w + f'(1 - g_w) \tag{3.45}$$

or

$$\frac{h_0 - h_w}{h_{0e} - h_w} = \frac{u}{u_e} \tag{3.46}$$

In order to obtain the rho-mu ratio C, ρ and μ in the boundary layer must be determined. ρ is obtained from the equation of state

$$p = \rho R T \tag{3.47}$$

$$R = \frac{\Re}{M} \tag{3.48}$$

$$M = \left(\sum_i \frac{c_i}{M_i}\right)^{-1} \tag{3.49}$$

---

[2]For adiabatic wall, $\left(k\frac{\partial T}{\partial y} + \rho D_{12} \sum_i h_i \frac{\partial c_i}{\partial y}\right)_w = 0$

An approximate temperature variation of the viscosity coefficient for nonreacting air, with a frozen chemical composition at standard conditions is given by *Hansen* in Ref. [11]

$$\mu = 1.462 \times 10^{-5} \frac{T^{\frac{1}{2}}}{1 + 112/T} \qquad [\frac{gm}{cm\,sec}] \qquad (3.50)$$

Since the chemically reacting effects are negligible below a temperature of $T = 5000$ K for the wide range of pressure, as shown in [11], Equation(3.50) is used for the calculation of the viscosity in this work. c_i in Eq.(3.49) is determined by the chemical equilibrium relations. Since the equilibrium composition is uniquely determined by any two state variables, c_i can be determined by the pressure and enthalpy. Since the pressure is assumed to be constant across the boundary layer, c_i can be calculated if the enthalpy is given.

3.2.2   Numerical Procedures

The problem of solving Eq.(3.41) with the boundary conditions Eqs.(3.43)- (3.44) is a two-point boundary value problem. This problem can be solved numerically. In this work, the shooting method([12]) is used with the fourth-order Runge-Kutta method to integrate the O.D.E.(3.41). Eq.(3.41) can be reduced to the following set of first order ordinary differential equations

$$F_1' = F_2 \qquad (3.51)$$

$$F_2' = F_3/C \qquad (3.52)$$

$$F_3' = -F_1 F_3/C \qquad (3.53)$$

where $F_1 = f$, $F_2 = f'$, and $F_3 = Cf''$. The boundary values for F_1 and F_2 at the wall are given by Eq.(3.43). The value of F_3 at the wall needs to be guessed first. With these boundary values, Eqs.(3.51)-(3.53) are integrated by the fourth-order Runge-Kutta method in the η direction to a large enough value of η such that $F_2(f'(\eta))$ becomes relatively constant with η. If F_2 does not satisfy the condition Eq.(3.44), then a new value of F_3 at the wall is chosen based on the discrepancy from the desired boundary value at large η.

The value of the rho-mu ratio $C = \frac{\rho\mu}{\rho_e\mu_e}$, which must be determined at each step of the integration, is calculated by the following procedures:

- Obtain h_0 using $f' = \frac{u}{u_e}$ from Eq.(3.46).

- Obtain $h = h_0 - \frac{1}{2}u^2$

- Obtain c_i and T from the chemical equilibrium calculation using h and p (see Appendix B).

- Obtain ρ from Eqs.(3.47)-(3.49).

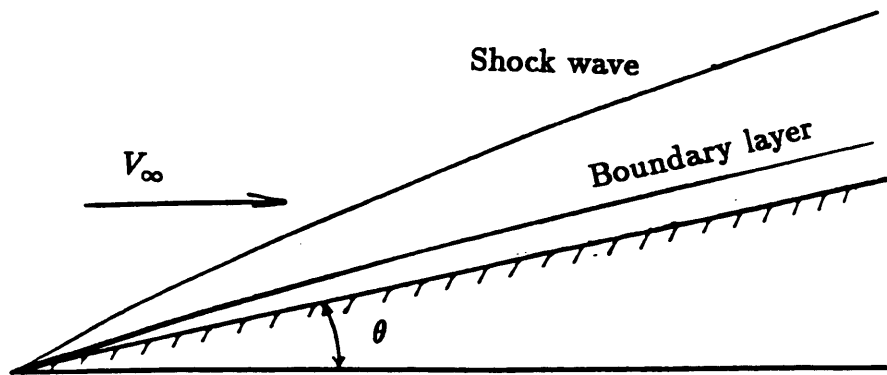- Obtain μ from (3.50).

Figure 3.1: Schematic of the flow over a wedge
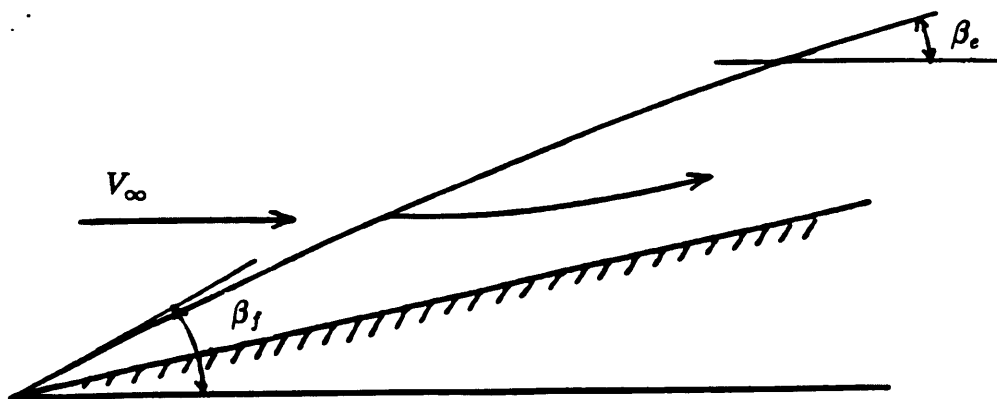
Figure 3.2: Schematic of nonequilibrium shock over a wedge
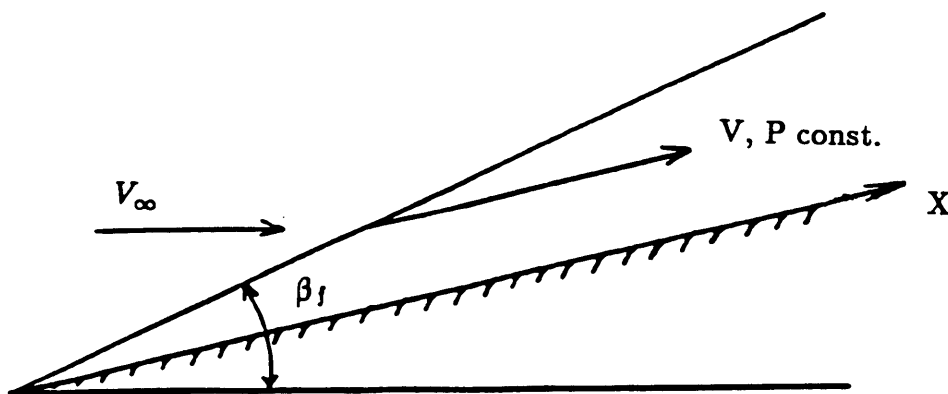
Figure 3.3: Simplified flow model over a wedge

Chapter 4

The Propagation of Electromagnetic Waves in Plasmas

This chapter develops an approach to evaluate the attenuation of electromagnetic waves propagating in a plasma. The plasma considered here is assumed to be isotropic, but non-uniform. The analysis of the propagation of electromagnetic waves in such a plasma is found in Refs.[1,13], for example.

4.1 Non-uniform, Isotropic Plasma

Maxwell's equations for the electromagnetic fields in a plasma are written as

$$\nabla \cdot \vec{D} = \varrho \tag{4.1}$$

$$\nabla \times \vec{E} = -\frac{\partial \vec{B}}{\partial t} \tag{4.2}$$

$$\nabla \times \vec{H} = \vec{J} + \frac{\partial \vec{D}}{\partial t} \tag{4.3}$$

$$\vec{D} = \varepsilon \vec{E} \tag{4.4}$$

$$\vec{B} = \mu \vec{H} \tag{4.5}$$

where ϱ is the free charge, and μ and ε represent the permiability and permittivity of the plasma, respectively. Assuming that the conduction current density $\vec{J}$ in the

plasma is proportional to the imposed electric field $\vec{E}$, $\vec{J}$ is simply related to $\vec{E}$ as

$$\vec{J} = \sigma \vec{E} \tag{4.6}$$

where σ is the conductivity. Then for time harmonic fields ($\vec{E}$, $\vec{B} \propto e^{i\omega t}$), Equations (4.2) and (4.3) become

$$\nabla \times \vec{E} = -i\omega\mu\vec{H} \tag{4.7}$$

$$\nabla \times \vec{H} = i\omega\varepsilon K_p\vec{E} \tag{4.8}$$

where ω is the frequency of the electromagnetic wave, and K_p is the effective dielectric coefficient

$$K_p = 1 + \frac{\sigma}{i\omega\varepsilon} \tag{4.9}$$

The equation of motion for electrons is given by

$$m_e\frac{\partial \vec{v_e}}{\partial t} + m_e\nu_{eff}\vec{v_e} = e\vec{E_0}e^{i\omega t} \tag{4.10}$$

where m_e is the electron mass, e is the electron charge, $\vec{v_e}$ is the electron velocity, and ν_{eff} is the effective collision frequency. If ν_{eff} is independent of v_e,

$$\vec{v_e} = \frac{e\vec{E_0}}{m_e(\nu_{eff} + i\omega)}e^{i\omega t} \tag{4.11}$$

Then the electron current density $\vec{J}$ is written as

$$
\begin{aligned}
\vec{J} &= n_e e\vec{v_e} \\
&= \frac{n_e e^2}{m_e(\nu_{eff} + i\omega)}\vec{E}
\end{aligned} \tag{4.12}
$$

Comparing Eqs.(4.6) and (4.12), the conductivity is obtained as

$$\sigma = \frac{n_e e^2}{m_e(\nu_{eff} + i\omega)} \tag{4.13}$$

Then the effective dielectric coefficient can be wriiten as

$$K_p = 1 - \left(\frac{\omega_p}{\omega}\right)^2 \left[\frac{1 + i\frac{\nu_{eff}}{\omega}}{1 + \left(\frac{\nu_{eff}}{\omega}\right)^2}\right] \tag{4.14}$$

28

where ω_p is the plasma frequency

$$\omega_p = \left(\frac{ne^2}{m_e \varepsilon_0} \right)^{\frac{1}{2}} \tag{4.15}$$

and ε has been assumed to have essentially the same value as the permittivity ε_0 in the vacuum. In this work, μ is also assumed to have the same value as μ_0 in the vacuum.

The equation of continuity is

$$\frac{\partial \varrho}{\partial t} + \nabla \cdot \vec{J} = 0 \tag{4.16}$$

In the time harmonic fields,

$$\begin{aligned} \frac{\partial \varrho}{\partial t} &= i\omega\varrho \\ &= i\omega\varepsilon\nabla \cdot \vec{E} \end{aligned} \tag{4.17}$$

Using Eqs.(4.17) and (4.6), Eq.(4.16) can be written as

$$\nabla \cdot (K_p \vec{E}) = 0 \tag{4.18}$$

or

$$\nabla \cdot \vec{E} = -\vec{E} \cdot \frac{\nabla K_p}{K_p} \tag{4.19}$$

Using Eq.(4.19), the wave equations of the electromagnetic waves in a non-uniform isotropic plasma are obtained from Eqs.(4.7) and (4.8):

$$\nabla^2 \vec{E} + k^2 K_p \vec{E} = -\nabla \left(\vec{E} \cdot \frac{\nabla K_p}{K_p} \right) \tag{4.20}$$

$$\nabla^2 \vec{H} + k^2 K_p \vec{H} = -\frac{\nabla K_p}{K_p} \times (\nabla \times \vec{H}) \tag{4.21}$$

where $k = \omega/c$, and the relation $\mu_0\varepsilon_0 = 1/c^2$ has been used.

4.2   Attenuation

This thesis considers only the attenuation of the electromagnetic waves propagating in the z-direction which is perpendicular to the wedge surface, as shown in
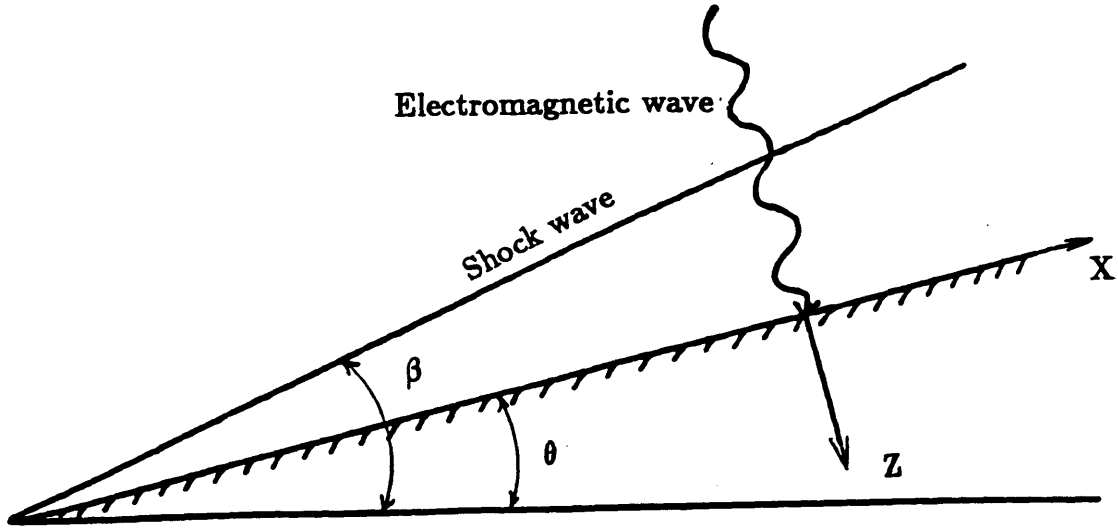
29

Figure 4.1: Schematic of Electromagnetic Wave Propagation over a Wedge

Fig. 4.1. This propagation path is considered to be the most desirable for communications since it minimizes the path length to the antenna.

Since the angle between the shock and the wedge $(\beta - \theta)$ is small, a few degrees at most, the direction of propagation is almost perpendicular to the shock. Since the flow properties in the inviscid region change only in the direction perpendicular to the shock, from the assumption in the previous chapter, the plasma properties are varying only in the direction of propagation. It is also assumed that, in the boundary layer, the local variation of the plasma properties in the x-direction is negligible compared with that in the z-direction. In this case, $\vec{E}$ and ∇K_p are orthogonal and Eq.(4.20) becomes

$$\frac{\partial^2 \vec{E}}{\partial z^2} + k^2 K_p \vec{E} = 0 \qquad (4.22)$$

If the value of K_p varies only slightly over the length of the electromagnetic wave, then the approximate solution of Eq.(4.22) is given by an expression of the form:

$$\vec{E} = \vec{E_0} e^{i\omega t} e^{-(A+iB)} \qquad (4.23)$$

where

$$A = k \int Re(\sqrt{K_p}) dz$$

$$= k \int \sqrt{\frac{|K_p| - Re(K_p)}{2}} dz \qquad (4.24)$$

30

$$B = k \int Im(\sqrt{K_p}) dz$$

$$= k \int \sqrt{\frac{|K_p| + Re(K_p)}{2}} dz \qquad (4.25)$$

and any reflected wave has been neglected. Since most of the attenuation is expected in the boundary layer, the thickness of which is of the order of centimeter, Eq.(4.23) will give a good approximation for electromagnetic waves with a wave length which is less than that order.

Since the electromagnetic wave is attenuated due to the term of e^{-A}, and K_p in this term is a function of ω_p and ν_{eff}, these values need to be given along the propagation path. ω_p is a function of electron density only as shown in Eq.(4.15). ν_{eff} is evaluated by the following expressions(Appendix C)in this work:

$$\nu_{eff} = \nu_{eff,m} + \nu_{eff,i}$$

$$\nu_{eff,m} = \frac{4\pi}{3} a^2 \bar{v} n_m \qquad (4.26)$$

$$\nu_{eff,i} = \pi \frac{e^4}{(\kappa T)^2} \bar{v} n_i \ln\left(0.37 \frac{\kappa T}{e^2 n_i^{\frac{1}{3}}}\right) \qquad (4.27)$$

where

$$\vec{v} = \left(\frac{8\kappa T}{\pi m}\right)^{\frac{1}{2}} \qquad (4.28)$$

κ is the Boltzmann constant, a is the radius of molecules, and n_m and n_i are the number densities of molecules and electrons, respectively.

31

Chapter 5

Numerical Results

This chapter presents the numerical results of the flow properties over a wedge and the attenuation of the electromagnetic waves propagating through the flow. The parameters considered in the calculations are shown in Table 5.1.

5.1 Flow Results

This section shows the chemical composition in the flow over a wedge. The flow field is divided into two regions:the inviscid region and the boundary layer. In the inviscid region, the finite rate chemistry is considered. The boundary layer is assumed to be laminar and in equilibrium.

5.1.1 Inviscid Region

The species distributions behind an oblique shock for various free stream velocities along the middle trajectory are shown in Figs 5.1- 5.5. The wedge angle θ is 15 degrees for all the cases.

As the velocity increases,the dissociation of oxygen is first observed at V=4 Km/s (M=13.1). The production of electrons becomes noticeable at V=6.5 Km/s (M=19.7), and at V=7.5 Km/s (M=24.7), the number density of electrons reaches the order of $10^6 m^{-3}$ approximately 10 m downstream from the shock.

Table 5.1: Calculation parameters

trajectory	wedge angle[deg]	wall temperature[K]	velocity[Km/s]
upper	15	1500	2 $\longrightarrow$ 7.5
middle	10	1500	2 $\longrightarrow$ 7.5
		1000	2 $\longrightarrow$ 7.5
	15	1500	2 $\longrightarrow$ 7.5
		2000	2 $\longrightarrow$ 7.5
	20	1500	2 $\longrightarrow$ 7.5
lower	15	1500	2 $\longrightarrow$ 7.5

Figure 5.6 shows the effect of trajectory on the species concentrations for V=6.5 Km/s, θ = 15 degrees, and T_W = 1500K. As the altitude becomes lower, the concentration of electrons increases.

Figure 5.7 shows the effect of wedge angle for V=6.5 km/s in the middle trajectory. The electron concentration increases significantly with the increase in wedge angle. For θ = 20 degrees, the number density of electrons increases rapidly within a few meters from the shock and reaches the order of $10^{15}m^{-3}$ approximately 7 m from the shock.

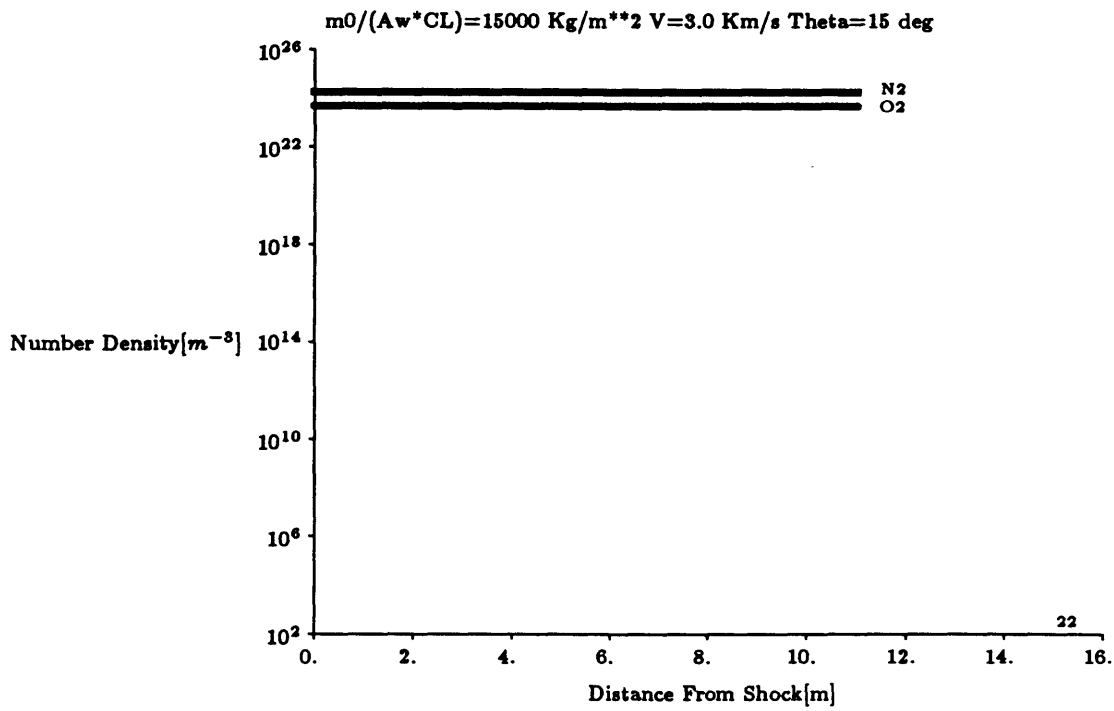mO/(Aw*CL)=15000 Kg/m**2 V=3.0 Km/s Theta=15 deg

Figure 5.1: Nonequilibrium species distributions behind a shock at V=3.0 Km/s

mO/(Aw*CL)=15000 Kg/m**2 V=4.0 Km/s Theta=15 deg

Figure 5.2: Nonequilibrium species distributions behind a shock at V=4.0 Km/s

m0/(Aw*CL)=15000 Kg/m**2 V=5.0 Km/s Theta=15 deg

Figure 5.3: Nonequilibrium species distributions behind a shock at V=5.0 Km/s

m0/(Aw*CL)=15000 Kg/m**2 V=6.5 Km/s Theta=15 deg
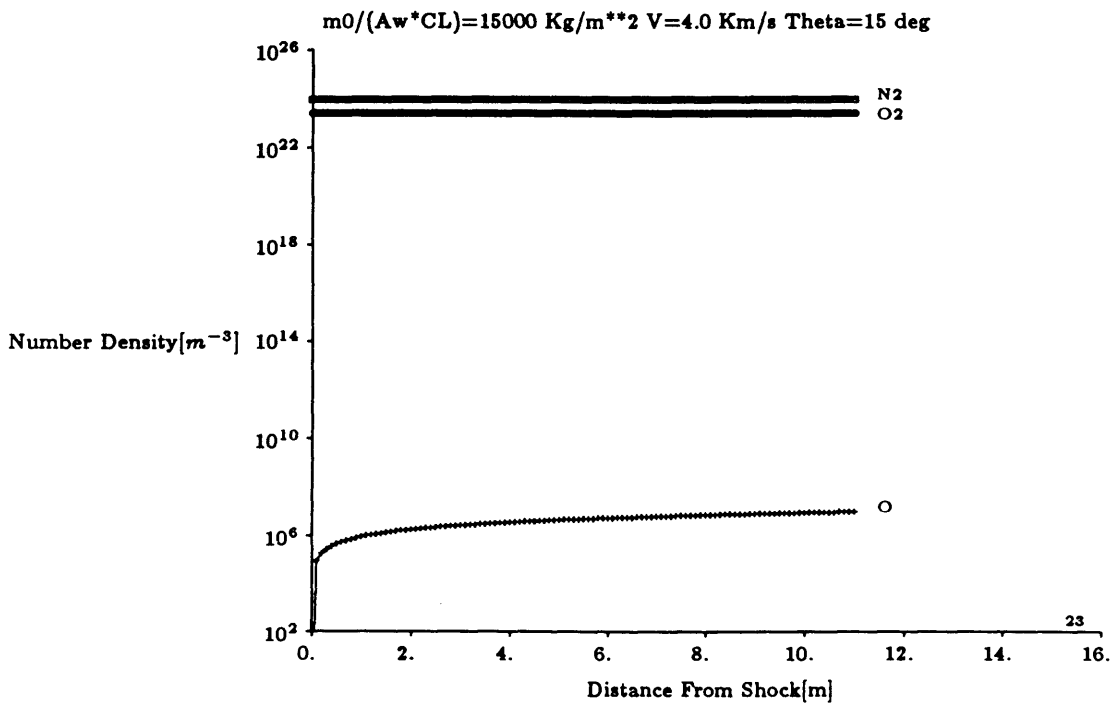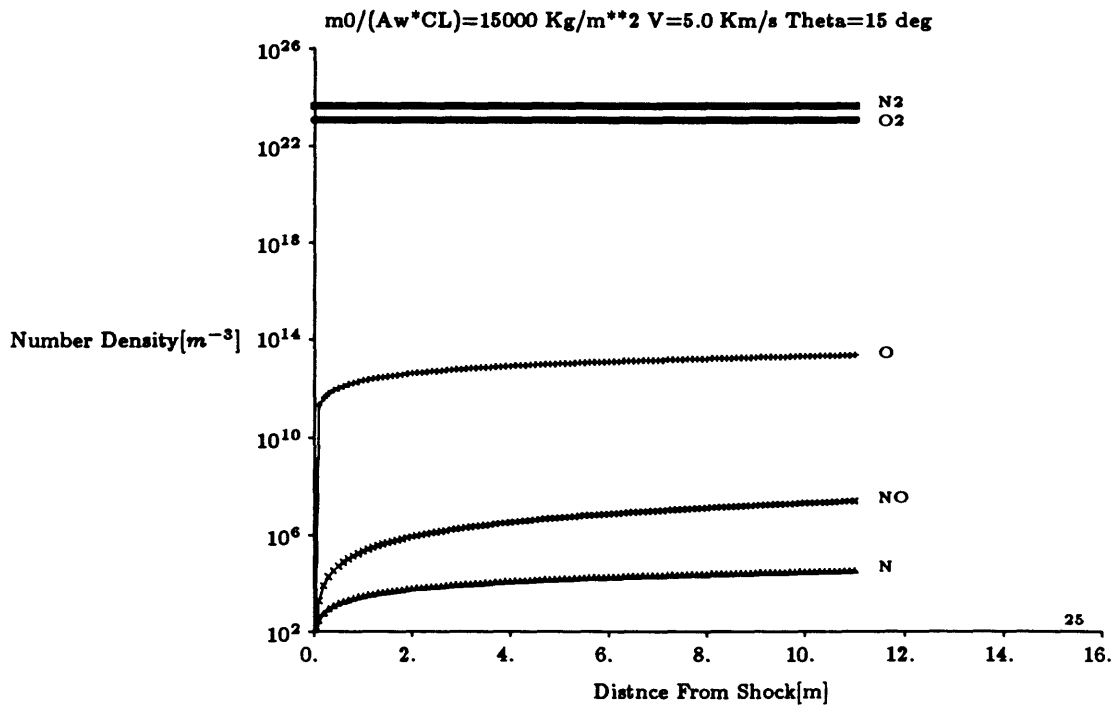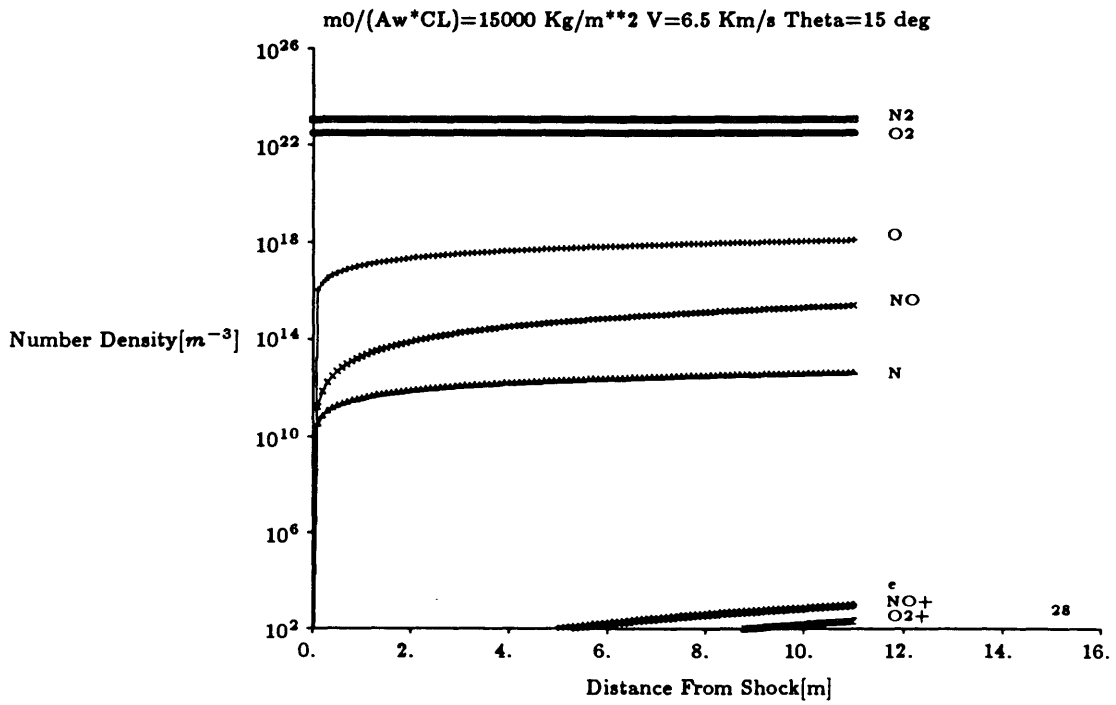
Figure 5.4: Nonequilibrium species distributions behind a shock at V=6.5 Km/s

Figure 5.5: Nonequilibrium species distributions behind a shock at V=7.5 Km/s

m0/(Aw*CL)=5000 Kg/m**2 V=6.5 Km/s Theta=15 deg

Number Density[m^{-3}]

N2
O2

O

NO

N

upper trajectory

Distance From Shock[m]

m0/(Aw*CL)=15000 Kg/m**2 V=6.5 Km/s Theta=15 deg

Number Density[m^{-3}]

N2
O2

O

NO

N

middle trajectory

e NO+
O2+

Distance From Shock[m]

m0/(Aw*CL)=25000 Kg/m**2 V=6.5 Km/s Theta=15 deg

Number Density[m^{-3}]

N2
O2

O

NO

N

lower trajectory

e NO+
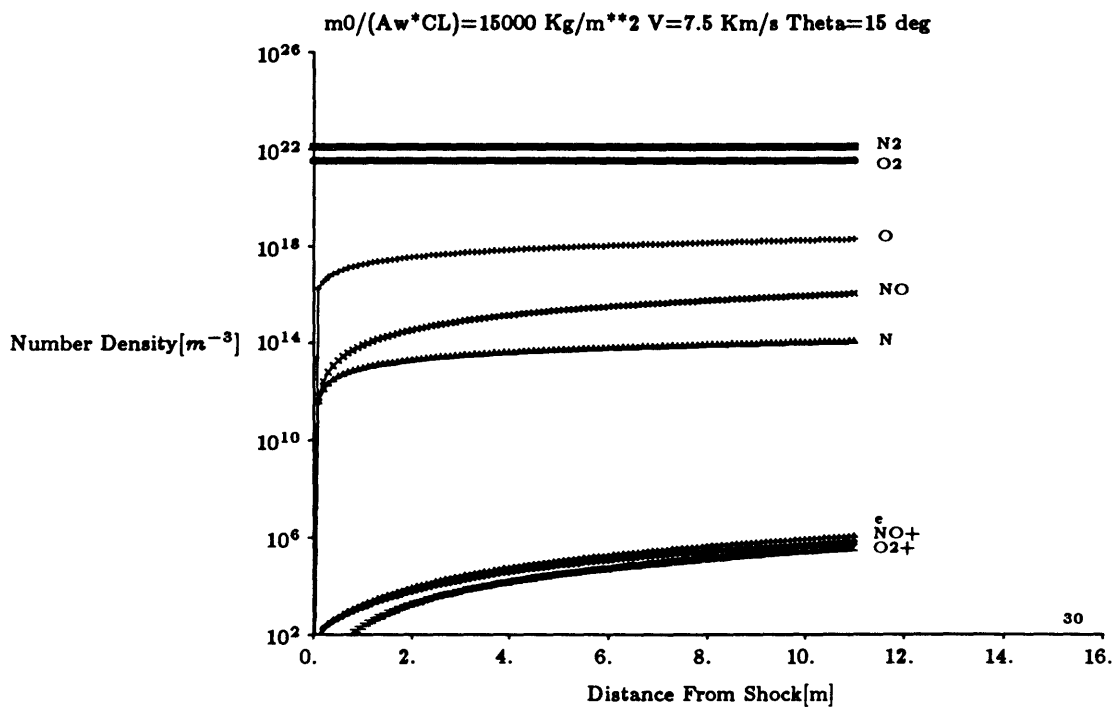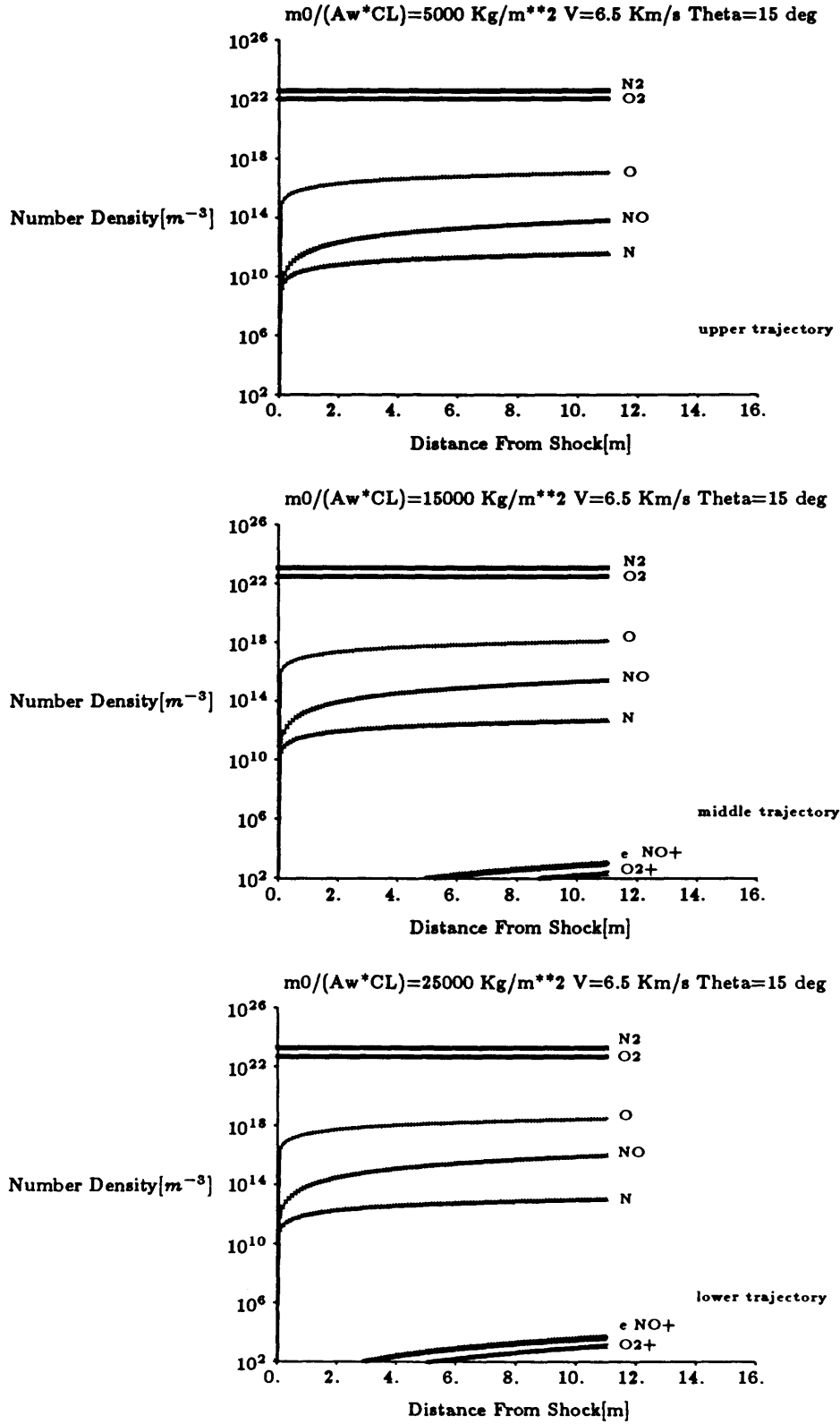O2+

Distance From Shock[m]

Figure 5.6: Effect of trajectory on nonequilibrium species distributions behind a shock at V=6.5 Km/s

37
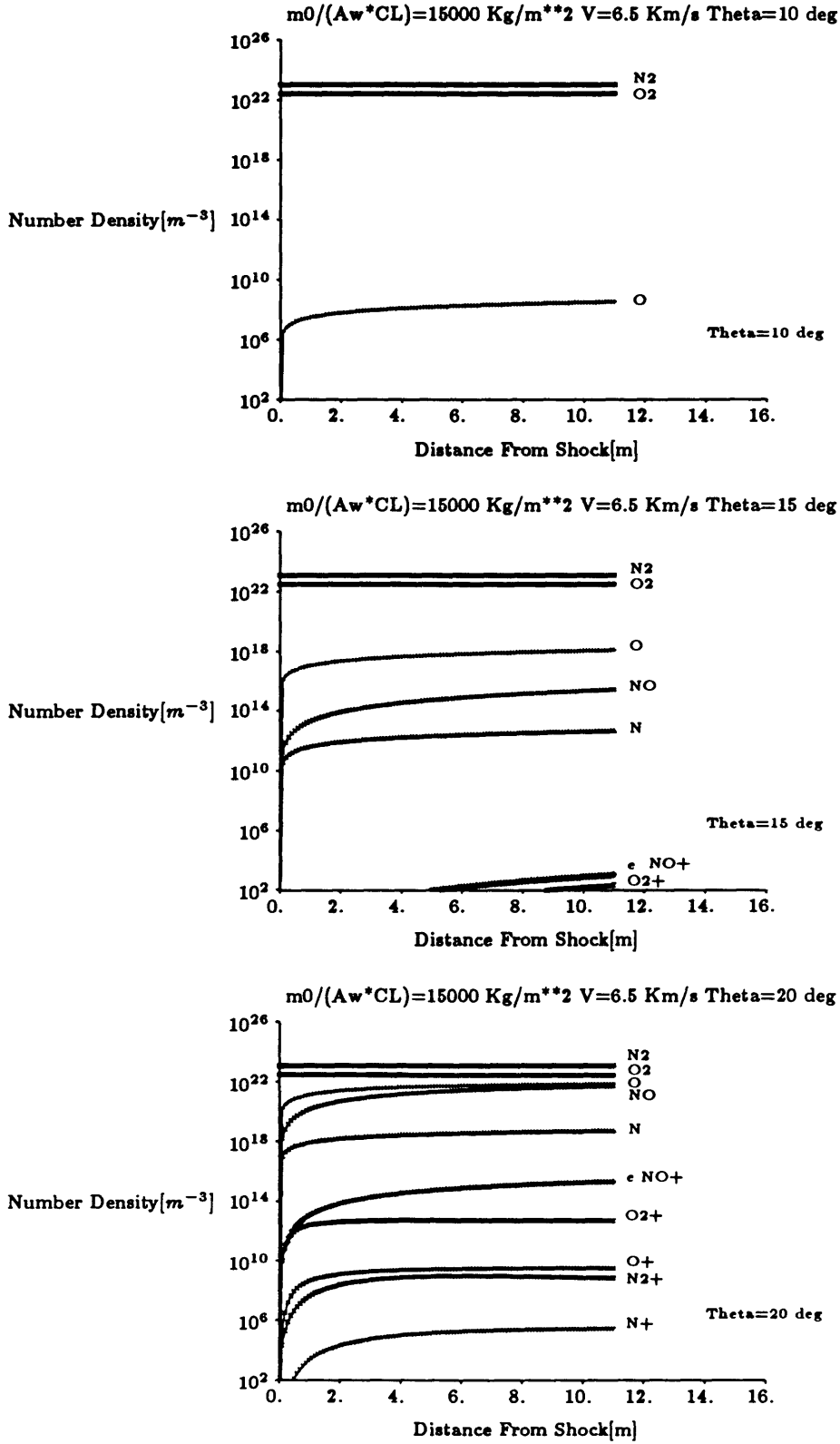
Figure 5.7: Effect of wedge angle on nonequilibrium species distributions behind a shock at V=6.5 Km/s

5.1.2 Boundary Layer

The velocity profiles, the temperature profiles, and the concentrations in the boundary layer 10 m downstream from the leading edge for various free stream velocities along the middle trajectory are shown in Figs 5.8- 5.17. The wedge angle and wall temperature are $\theta = 15$ degrees and $T_W = 1500$ K, respectively.

The boundary layer thickness increases with velocity from about 1 cm at V=3.0 Km(M=10.0) to about 8 cm at V=7.5 Km/s(M=24.7). The maximum number density of electrons reaches the order of $10^{16} m^{-3}$ at V=5.0 Km/s, and beyond that velocity, it does not increase significantly because of the rapid decrease of the air density along the trajectory. The region with high electron density,however, increases significantly with the increase in the boundary layer thickness at high velocities.

mO/(Aw*CL)=15000 Kg/m**2 V=3.0 Km/s Theta=15 deg Tw=1500 K

T[K]   U[m/s]

Y[m]

Velocity[m/s], Temperature[K]

Figure 5.8: Velocity and temperature profiles in a boundary layer at V=3.0 Km/s

mO/(Aw*CL)=15000 Kg/m**2 V=3.0 Km/s Theta=15 deg Tw=1500 K

NO   O2 N2

Y[m]

O

e NO+   N

Number Density $[m^{-3}]$

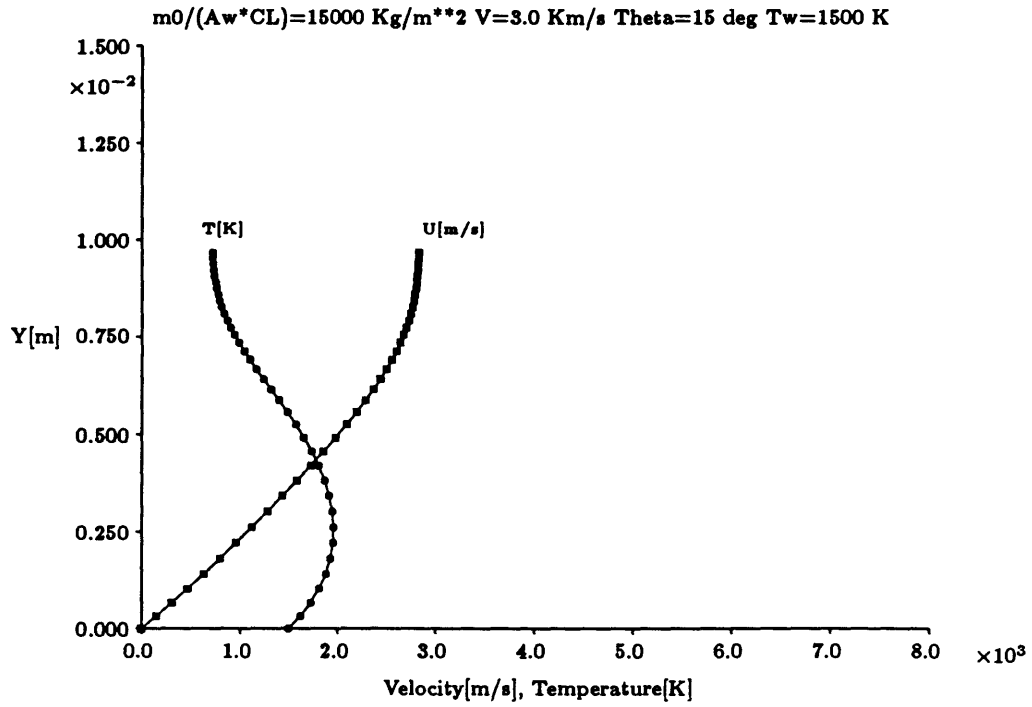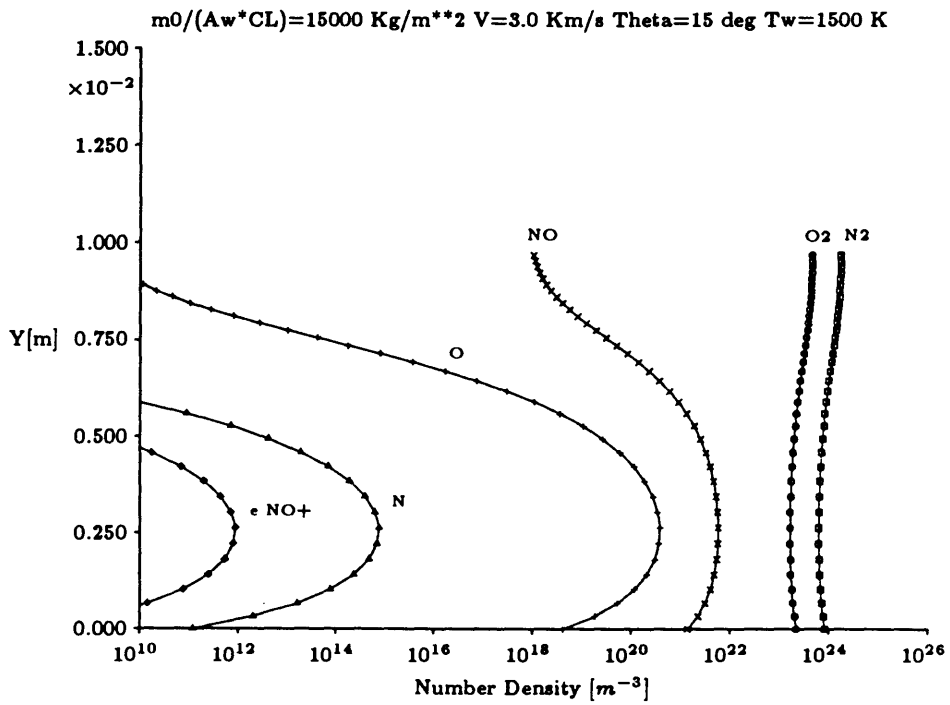Figure 5.9: Species concentrations in a boundary layer at V=3.0 Km/s
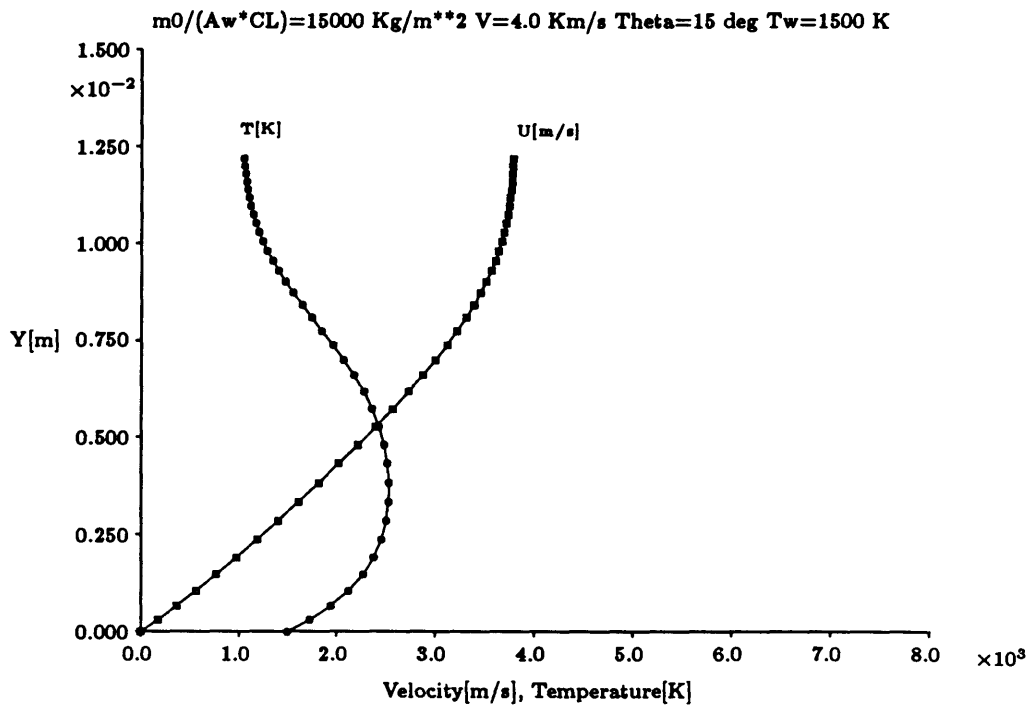
Figure 5.10: Velocity and temperature profiles in a boundary layer at V=4.0 Km/s
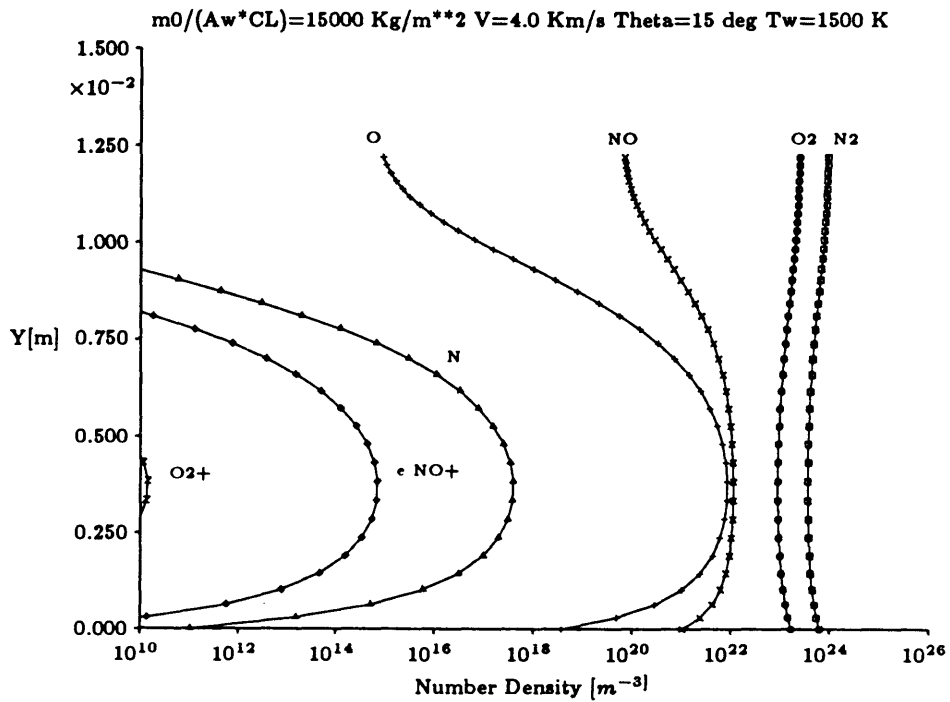
Figure 5.11: Species concentrations in a boundary layer at V=4.0 Km/s

m0/(Aw*CL)=15000 Kg/m**2 V=5.0 Km/s Theta=15 deg Tw=1500 K
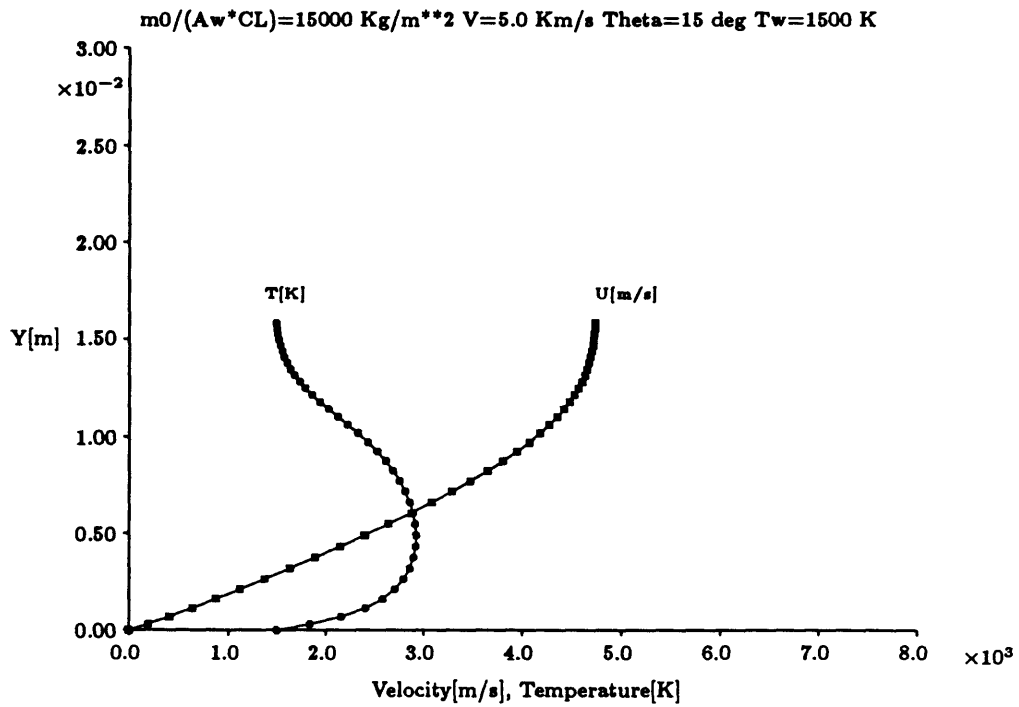
Figure 5.12: Velocity and temperature profiles in a boundary layer at V=5.0 Km/s

m0/(Aw*CL)=15000 Kg/m**2 V=5.0 Km/s Theta=15 deg Tw=1500 K
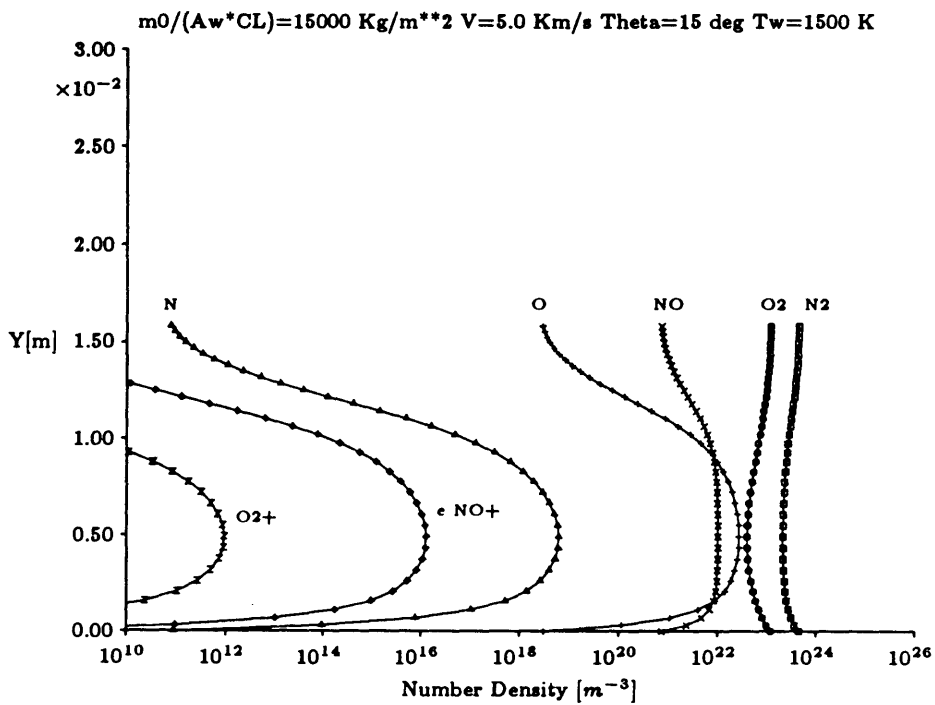
Figure 5.13: Species concentrations in a boundary layer at V=5.0 Km/s

m0/(Aw*CL)=15000 Kg/m**2 V=6.5 Km/s Theta=15 deg Tw=1500 K
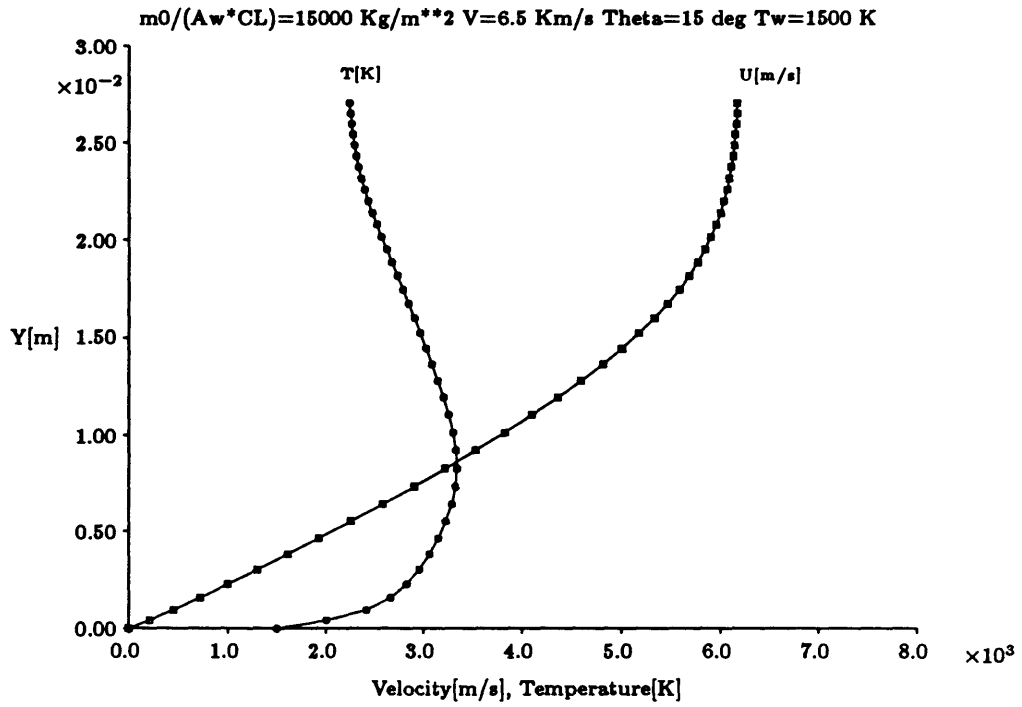
Figure 5.14: Velocity and temperature profiles in a boundary layer at V=6.5 Km/s

m0/(Aw*CL)=15000 Kg/m**2 V=6.5 Km/s Theta=15 deg Tw=1500 K
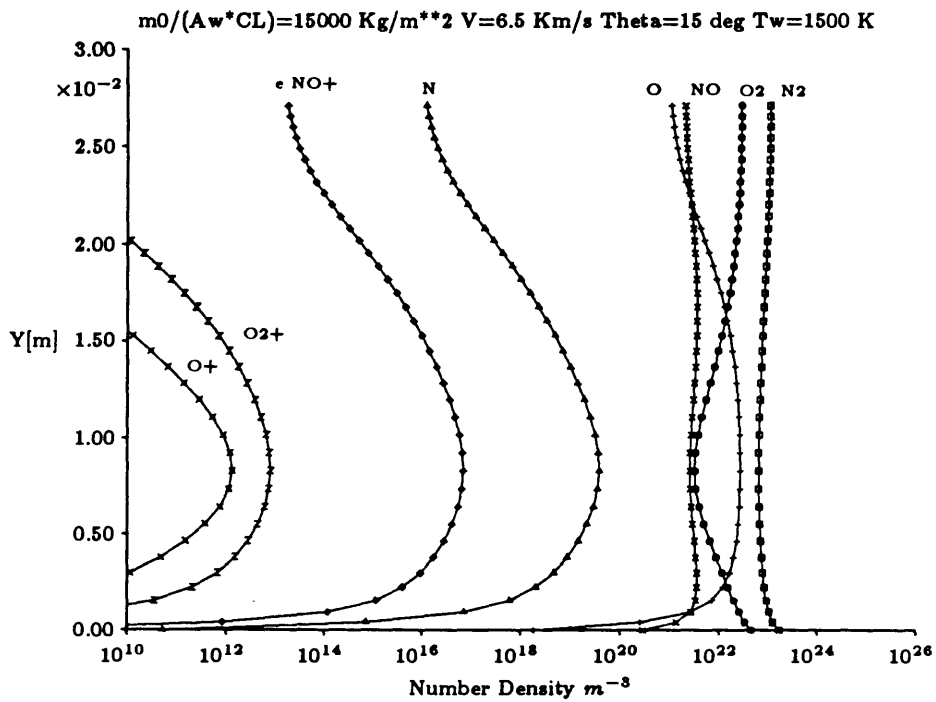
Figure 5.15: Species concentrations in a boundary layer at V=6.5 Km/s

m0/(Aw*CL)=15000 Kg/m**2 V=7.5 Km/s Theta=15 deg Tw=1500 K

T[K] ... U[m/s]

Y[m]

Velocity[m/s], Temperature[K]

×10³
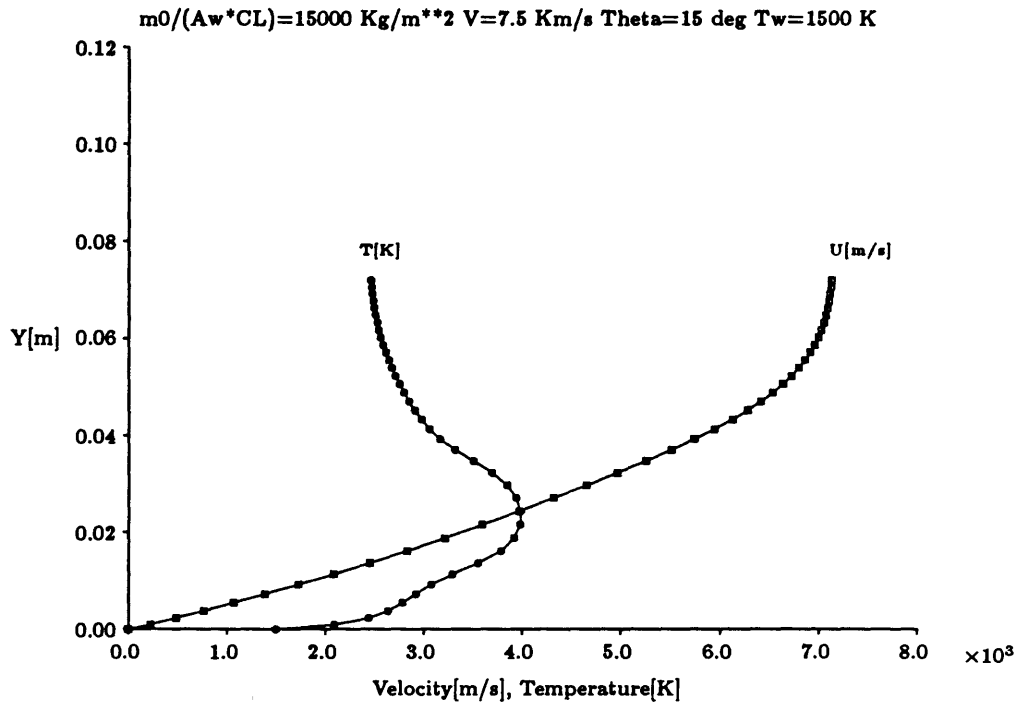
Figure 5.16: Velocity and temperature profiles in a boundary layer at V=7.5 Km/s

m0/(Aw*CL)=15000 Kg/m**2 V=7.5 Km/s Theta=15 deg Tw=1500 K

e NO+   N   NO O O2 N2

Y[m]

O2+

N2+

N+   O+

Number Density [m⁻³]
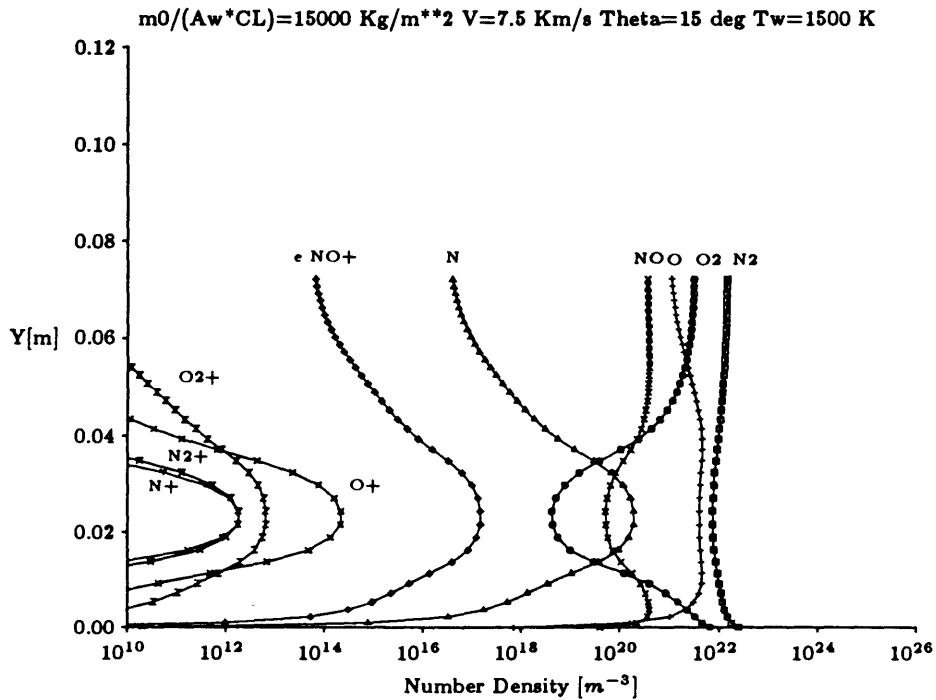
Figure 5.17: Species concentrations in a boundary layer at V=7.5 Km/s

44

Figure 5.18 shows the effect of trajectory on the velocity and temperature profiles in a boundary layer at V=6.5 Km(M=19.7) for the wedge angle $\theta = 15°$ and the wall temperature $T_W = 1500$ K. Figure 5.19 shows the effect of trajectory on the concentrations in a boundary layer for the same conditions. As the altitude decreases, the boundary layer thickness decreases and the maximum electron density increases.

Figure 5.20 shows the effect of wedge angle on the velocity and temperature profiles in a boundary layer at V=6.5 Km(M=19.7) in the middle trajectory for $T_W = 1500K$. Figure 5.21 shows the effect of wedge angle on the concentrations in a boundary layer for the same conditions. As the wedge angle increases, the boundary layer thickness decreases and the electron density increases significantly.

Figure 5.22 shows the effect of wall temperature on the velocity and temperature profiles in a boundary layer at V=6.5 Km(M=19.7) in the middle trajectory for $\theta = 15°$. Figure 5.23 shows the effect of wall temperature on the concentrations for the same conditions. The variation of the boundary layer thickness with the wall temperature is very small for the range $1000K \leq T_W \leq 2000K$. The increase of the electron density with the increase in wall temperature is noticeable only in the vicinity of the wall.

Figure 5.18: Effect of trajectory on Velocity and temperature profiles in a boundary layer at V=6.5 Km/s
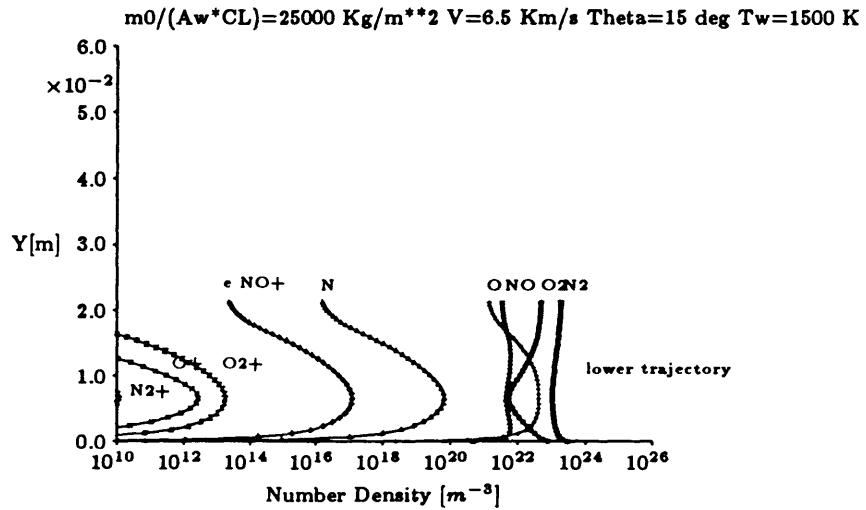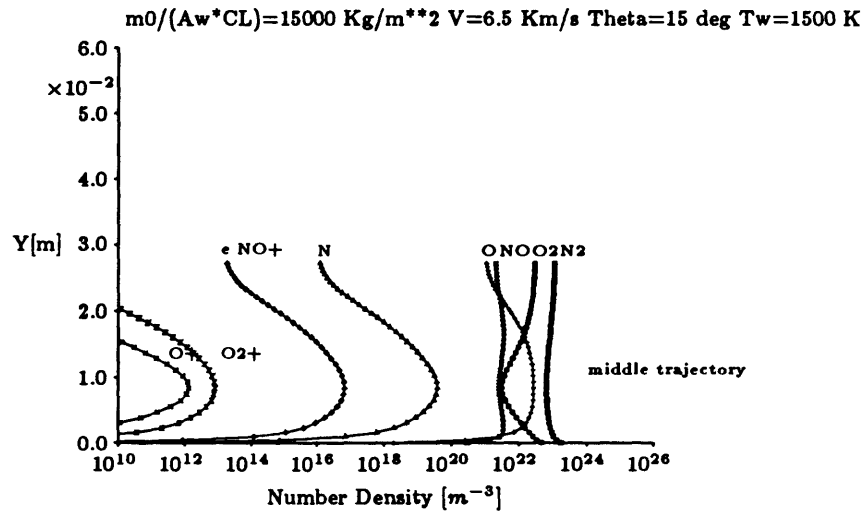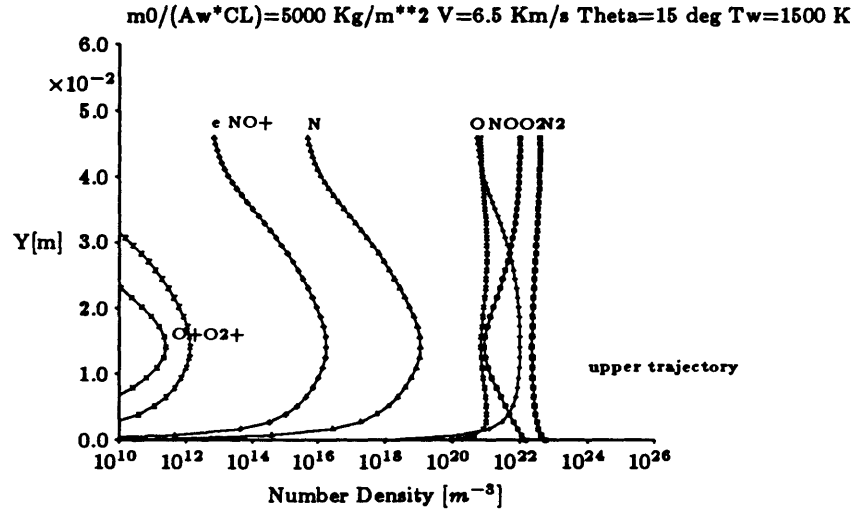
Figure 5.19: Effect of trajectory on concentrations in a boundary layer at V=6.5 Km/s

m0/(Aw*CL)=15000 Kg/m**2 V=6.5 Km/s Theta=10 deg Tw=1500 K

m0/(Aw*CL)=15000 Kg/m**2 V=6.5 Km/s Theta=1500 K Tw=1500 K

m0/(Aw*CL)=15000 Kg/m**2 V=6.5 Km/s Theta=20 deg Tw=1500 K

Figure 5.20: Effect of wedge angle on Velocity and temperature profiles in a boundary layer at V=6.5 Km/s

m0/(Aw*CL)=15000 Kg/m**2 V=6.5 Km/s Theta=10 deg Tw=1500 K

O   NO   O2N2

Y[m]   3.0

e NO+   N

O   O2+

$\theta = 10 deg$

Number Density $[m^{-3}]$

m0/(Aw*CL)=15000 Kg/m**2 V=6.5 Km/s Theta=15 deg Tw=1500 K

Y[m]   3.0

e NO+   N   O NO O2N2

O   O2+

$\theta = 15 deg$

Number Density $[m^{-3}]$

m0/(Aw*CL)=15000 Kg/m**2 V=6.5 Km/s Theta=20 deg Tw=1500 K

Y[m]   3.0

O2+   e NO+   N   NO   N2

O+

N2+   O   O

$\theta = 20 deg$

Number Density $[m^{-3}]$

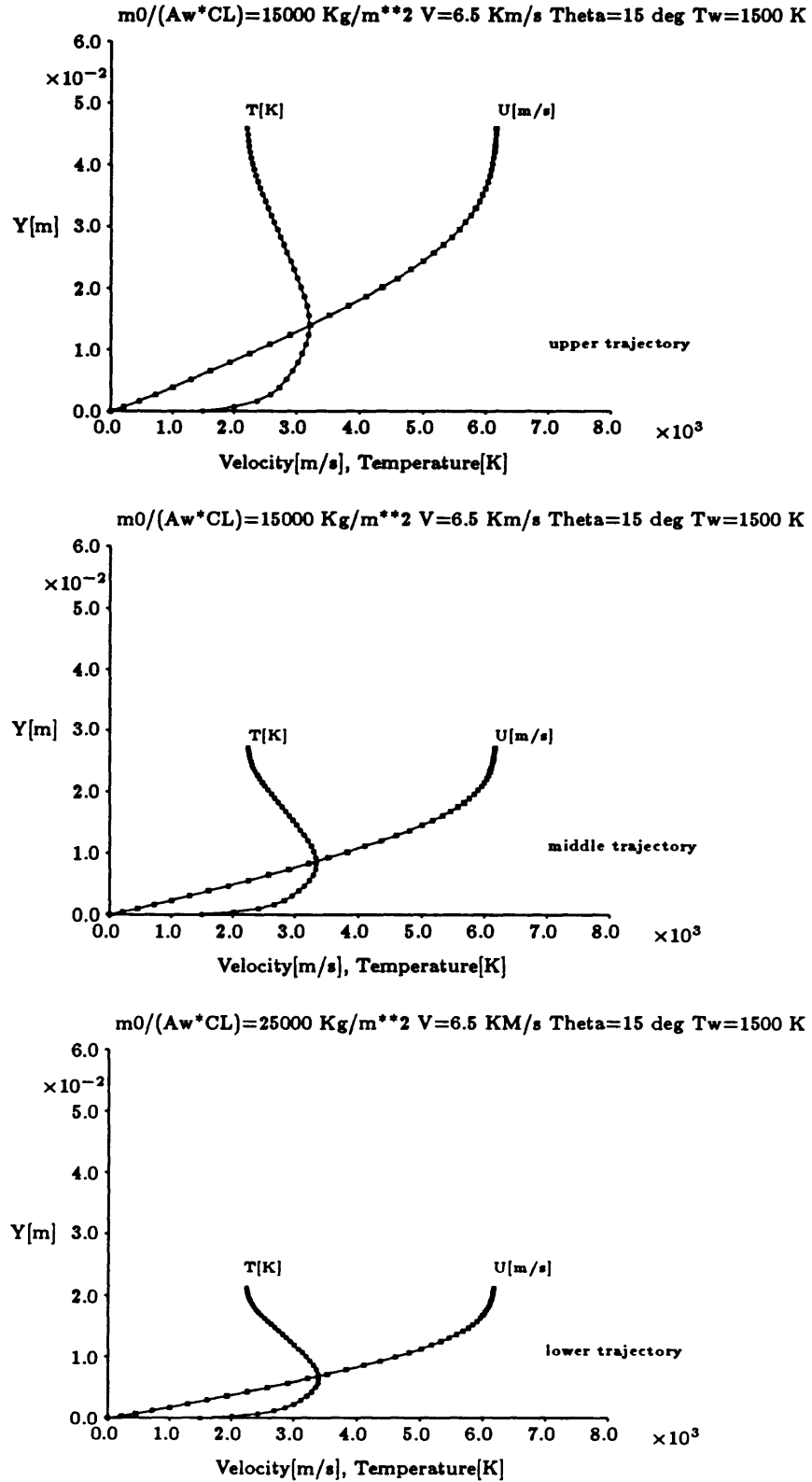Figure 5.21: Effect of wedge angle on concentrations in a boundary layer at V=6.5 Km/s

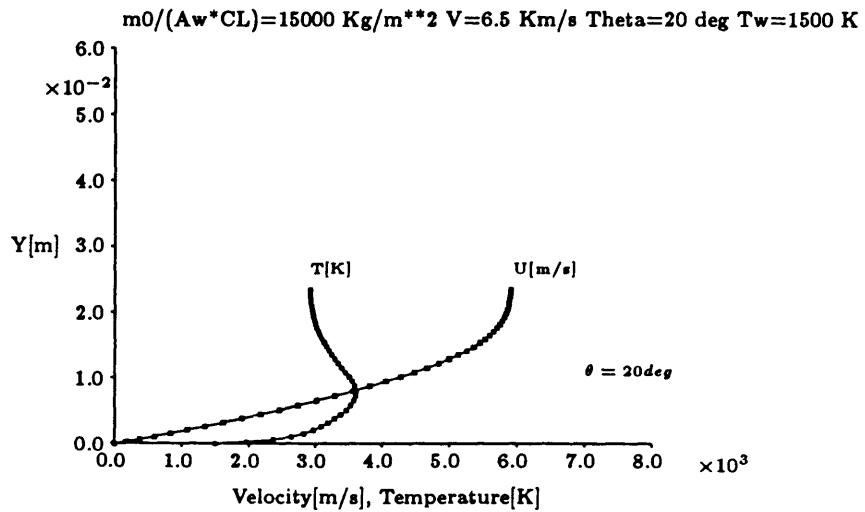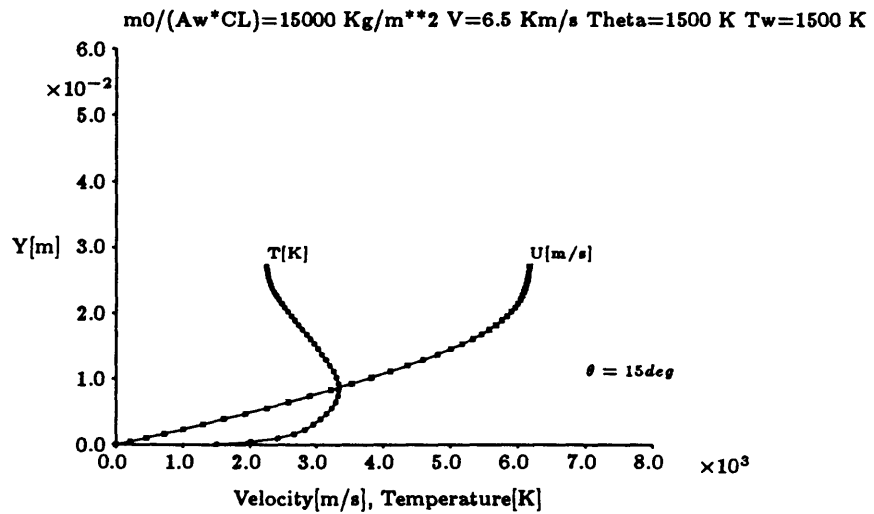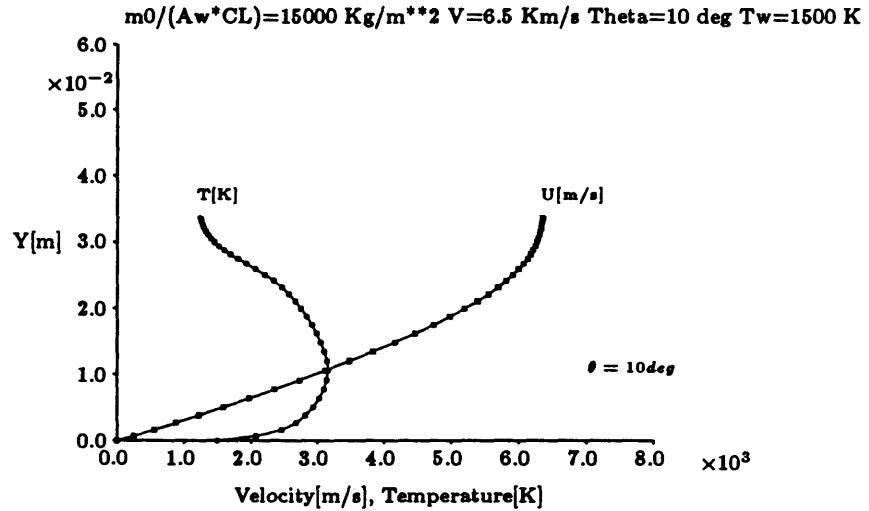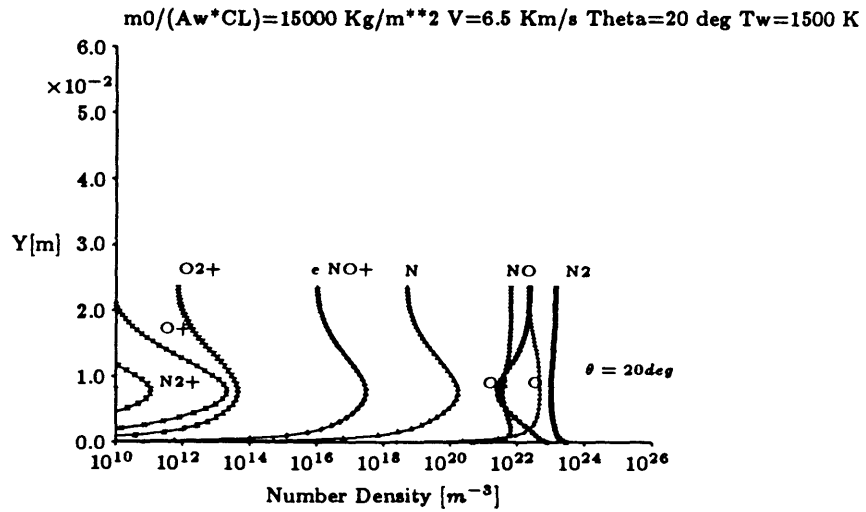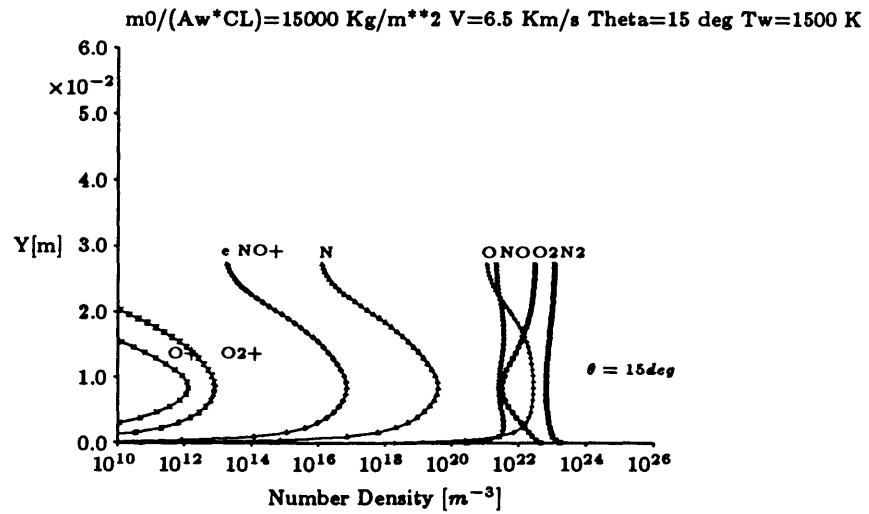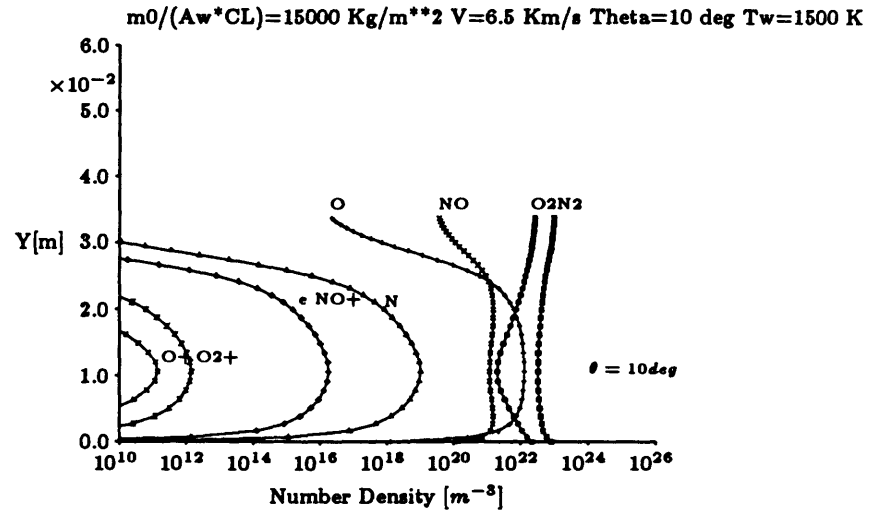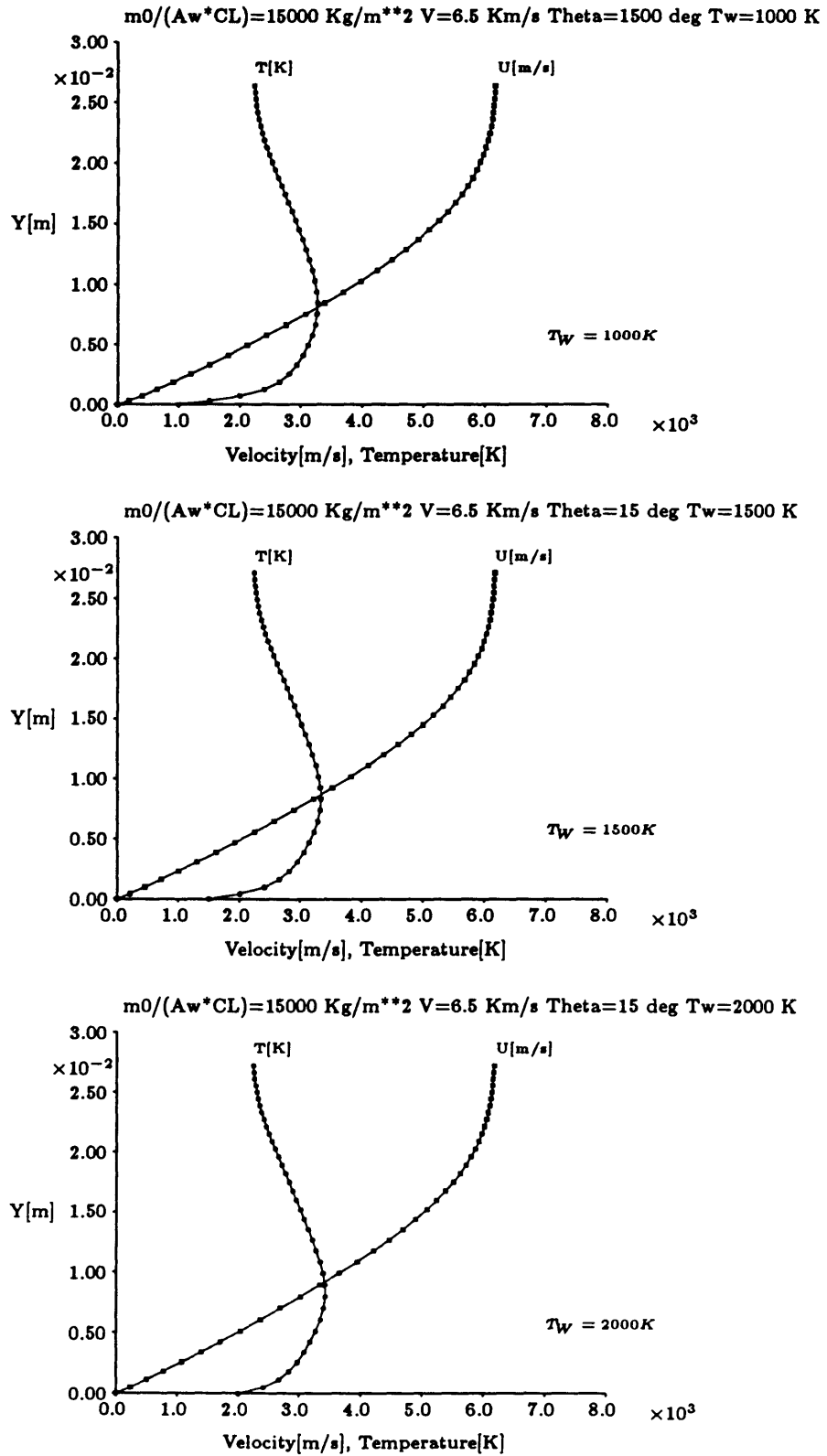Figure 5.22: Effect of wall temperature on Velocity and temperature profiles in a boundary layer at V=6.5 Km/s
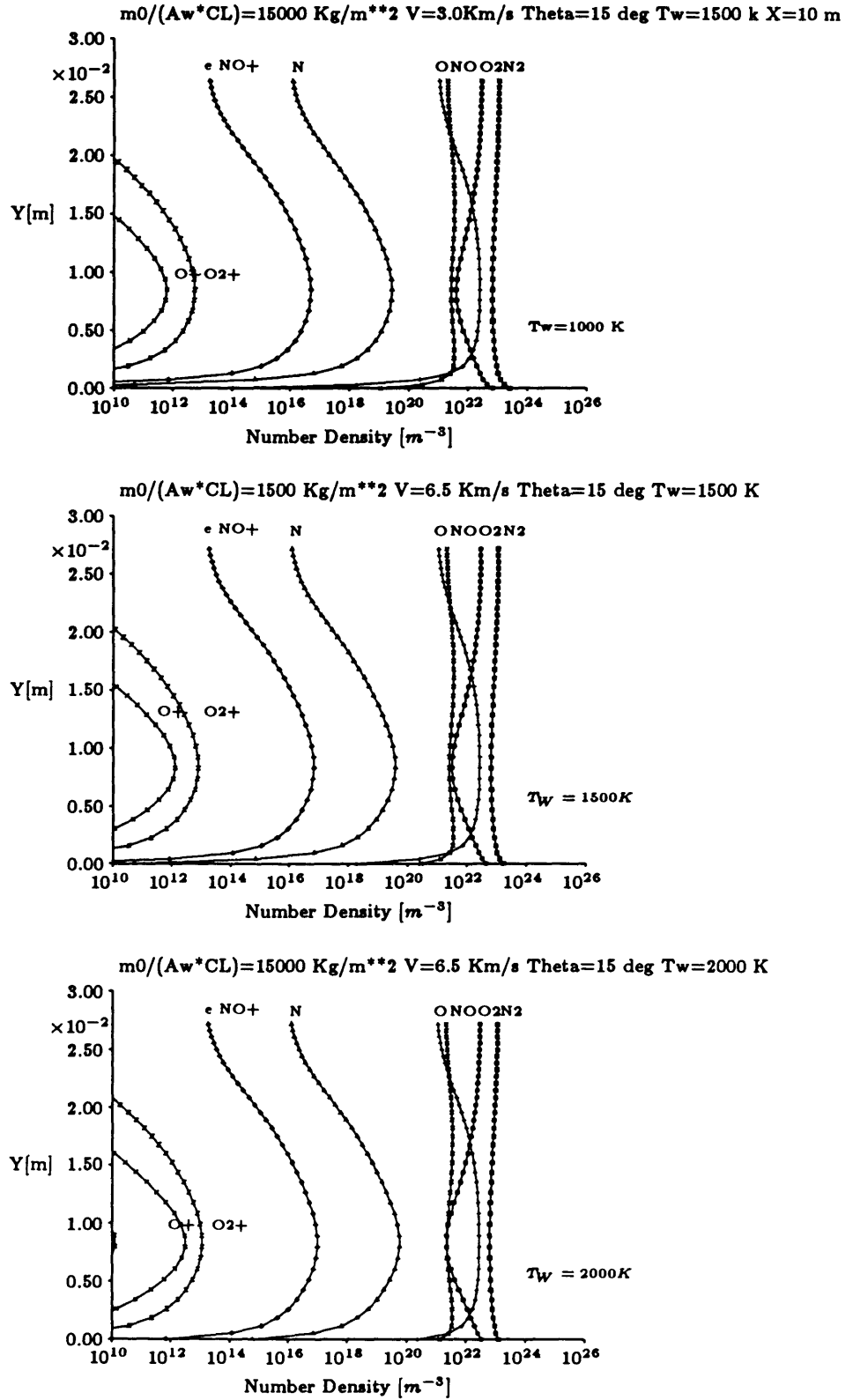
Figure 5.23: Effect of wall temperature on concentrations in a boundary layer at V=6.5 Km/s

5.2 Attenuation of Electromagnetic Waves

This section presents the numerical results of the attenuation of the power of the electromagnetic waves propagating through the plasma over a wedge. The location of antenna is tentatively chosen to be 10 m from the leading edge.

Figure 5.24 shows the effect of trajectory on the attenuation for $\theta = 15°$ and $T_W = 1500K$. In this figure, the attenuation is shown with the frequency of the electromagnetic waves for various velocities. The attenuation becomes significant above V=5.0 Km/s(M=16.0) for all the trajectories below some frequency, which increases with decreasing altitude. This critical frequency is 2.4 GHz for the upper, 4 GHz for the middle, and 6.3 GHz for the lower trajectory. The magnitude of attenuation becomes 3 dB at about V=6.5 Km/s(M=20) and reaches about 10 dB at V=7.5 Km/s(M=25) for 1 GHz. This result shows that electromagnetic waves with radio frequencies in S band(2-4 GHz) or lower are strongly attenuated along the upper trajectory and those in C band(4-6 GHz) or lower are attenuated along the middle and lower trajectories. On the other hand, no noticeable attenuation is observed in X band(8-12 GHz).

Figure 5.25 shows the effect of wedge angle on the attenuation along the middle trajectory for $T_W = 1500K$. The attenuation increases significantly with the increase in wedge angle and the critical frequency increases from 2.4 GHz for $\theta = 10°$ to 10 GHz for $\theta = 20°$. This result shows that for $\theta = 20°$, communications with X band are also attenuated at high velocities. The drastic increase of the attenuation with increased wedge angle corresponds to the rapid increase of the electron density in the inviscid region and the outer part of the boundary layer. On the other hand, the critical velocity above which the attenuation becomes significant does not change considerably with wedge angle.

Figure 5.26 shows the effect of wall temperature on the attenuation along the middle trajectory for $\theta = 15°$. The attenuation for each velocity increases with increased wall temperature; however, the critical frequency is relatively constant.

The variation of the attenuation with velocity for an electromagnetic wave with 1 GHz is shown in Figures 5.27- 5.29. Figure 5.27 shows the effect of trajectory on the attenuation for $\theta = 15°$ and $T_W = 1500K$. A considerable difference is found between the upper and middle trajectories. This result clearly shows the advantage of a high altitude.

Figure 5.28 shows the effect of wedge angle on the attenuation along the middle trajectory for $T_W = 1500K$. The attenuation increases rapidly with increasing wedge angle above V=4.0 Km/s; the wedge angle above 10 degrees is not desirable.

Figure 5.29 shows the effect of wall temperature on the attenuation along the middle trajectory for $\theta = 15°$. Although the effect of wall temperature for the considered range $1000K \leq T_W \leq 2000K$ is relatively small compared with the effect of wedge angle, a cooled wall is effective in alleviating the attenuation.

The frequency range considered here is from 0.1 GHz to 10 GHz and the corresponding wave length is from 3 m to 3 cm. On the other hand, the boundary layer thickness, in which the major attenuation occurs, is from 1 cm to 8 cm. Therefore Eq.(4.23), which is obtained assuming that the dielectric coefficient varies slightly over the length of the electromagnetic wave, may not be accurate except at high frequencies near 10 GHz. However, since the variation of attenuation with radio frequency is very drastic and the magnitude of attenuation at lower frequencies is very large, the uncertainty due to the assumption used for Eq.(4.23) will not change the essential results significantly.

Since a received power is proportional to the power from the transmitter and the aperture of the antenna, the compensation of the attenuation requires an increase in the power or antenna size. These compensations would be,however, unacceptable below the critical frequency since the maximum power loss is expected to be more than 90 %. Therefore the radio frequency will need to be higher than the critical frequency.

On the other hand, higher radio frequencies may require a larger size of transmitter and receiver. In addition, the absorption of the electromagnetic waves due to the water vapor and oxygen in the atmosphere becomes important above 20 GHz [1]. Thus the selection of the radio frequency and antenna location, which may be restricted by other constraints such as structures and cooling system, will be an important issue for the vehicle design.

m0/(Aw*CL)=5000 Kg/m**2 Theta=15 deg Tw=1500 K X=10 m

upper trajectory

m0/(Aw*CL)=15000 Kg/m**2 Theta=15 deg Tw=1500 K X=10 m

middle trajectory

m0/(Aw*CL)=25000 Kg/m**2 Theta=15 deg Tw=1500 K X=10 m

lower trajectory
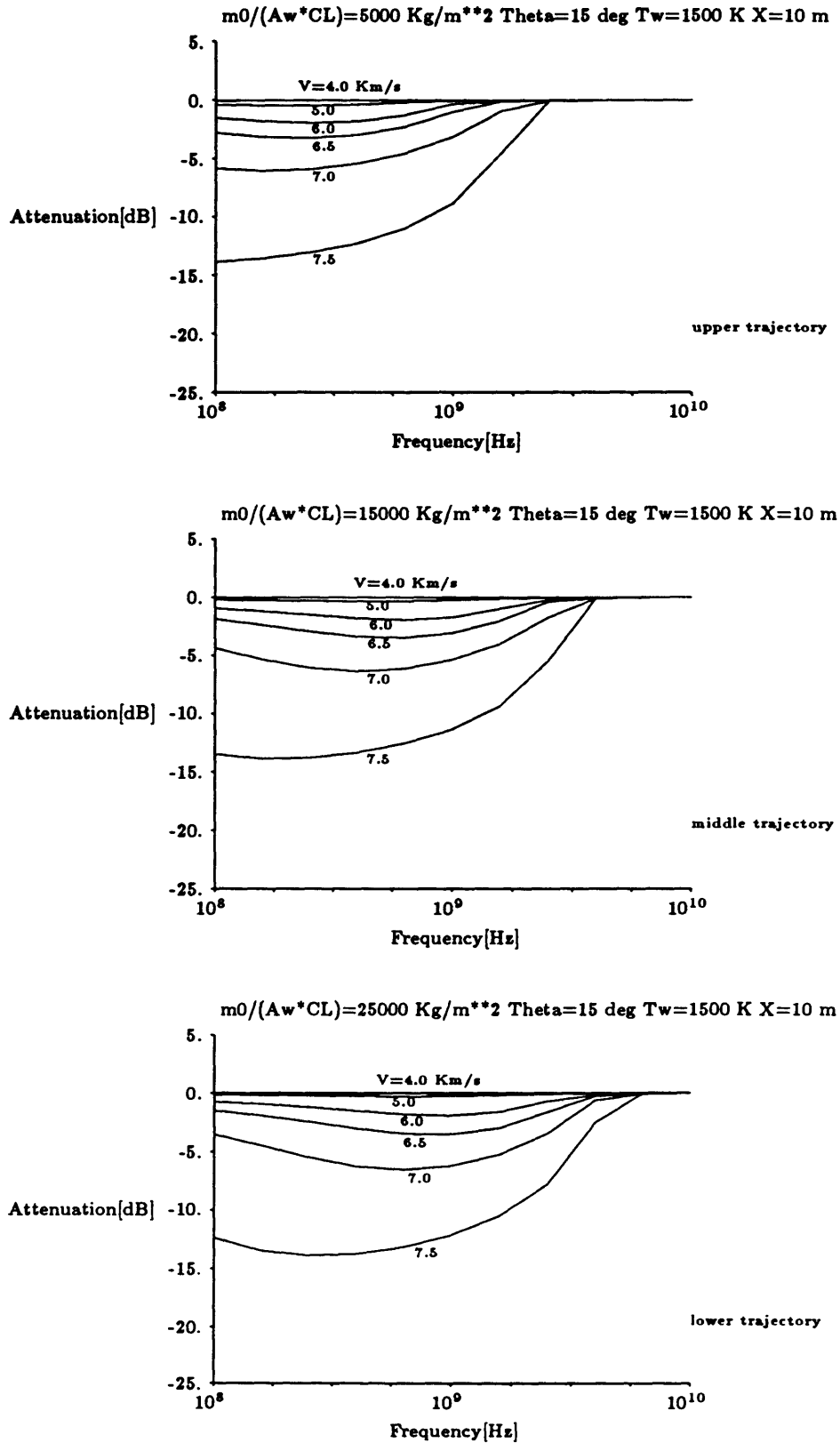
Figure 5.24: Effect of trajectory on the attenuation of electromagnetic waves
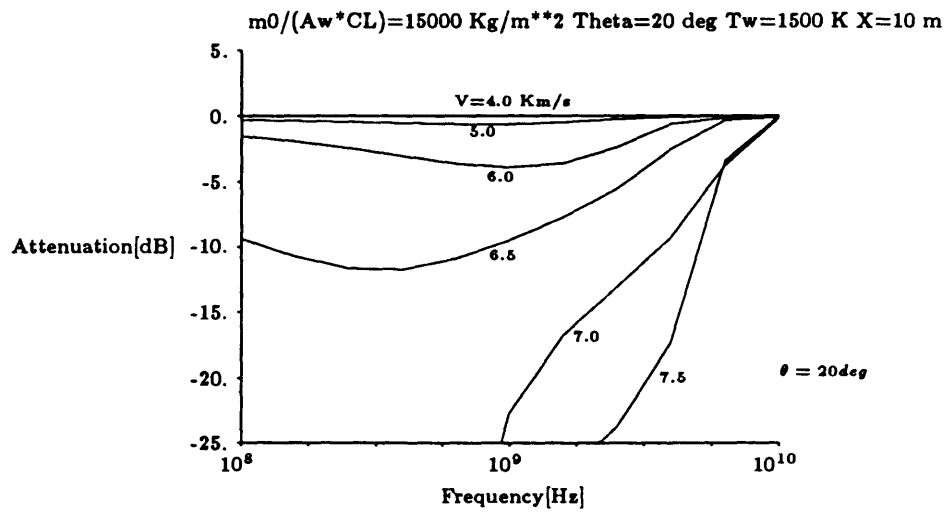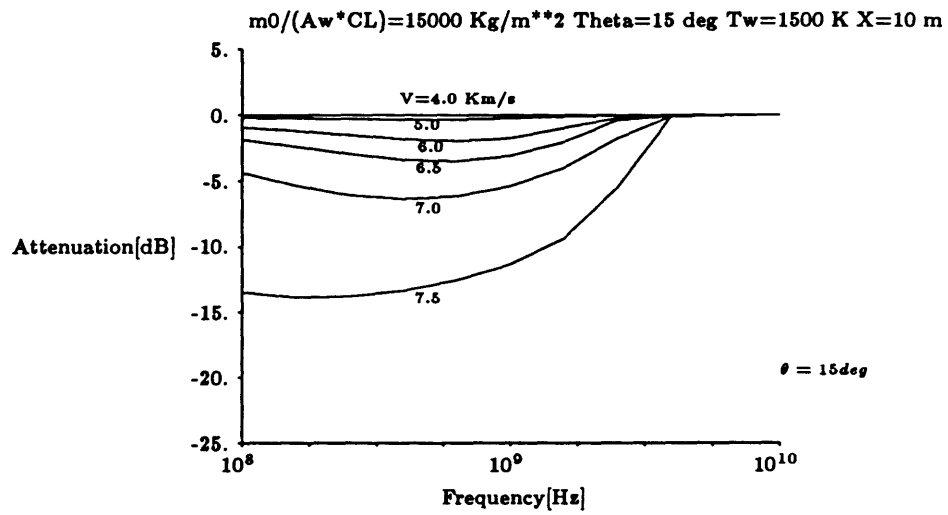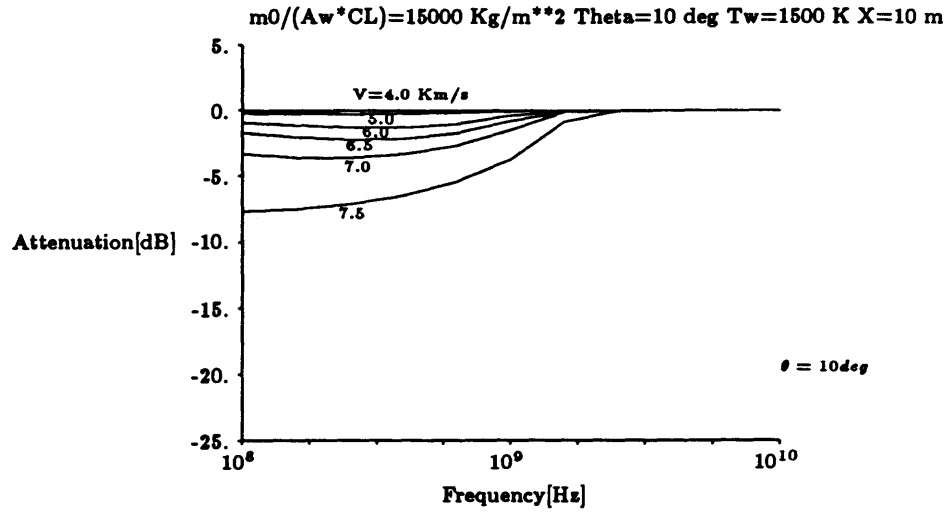
Figure 5.25: Effect of wedge angle on the attenuation of electromagnetic waves
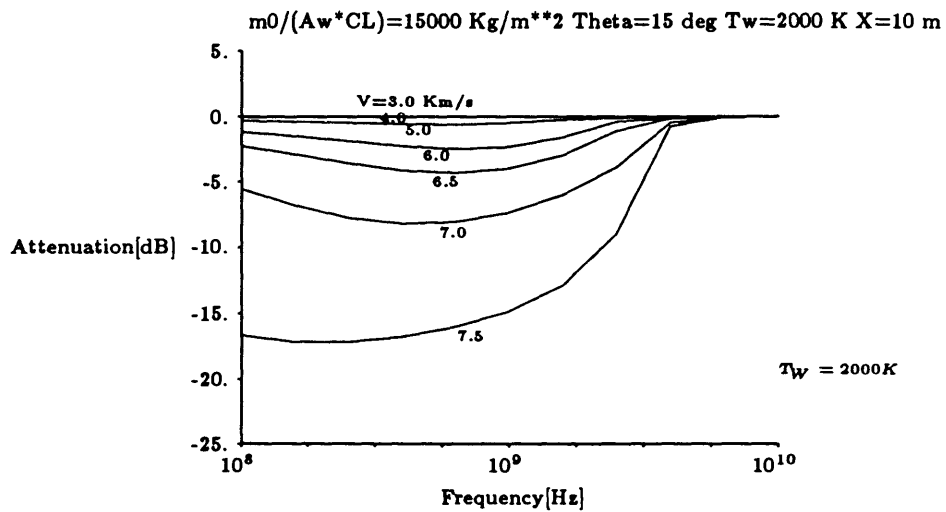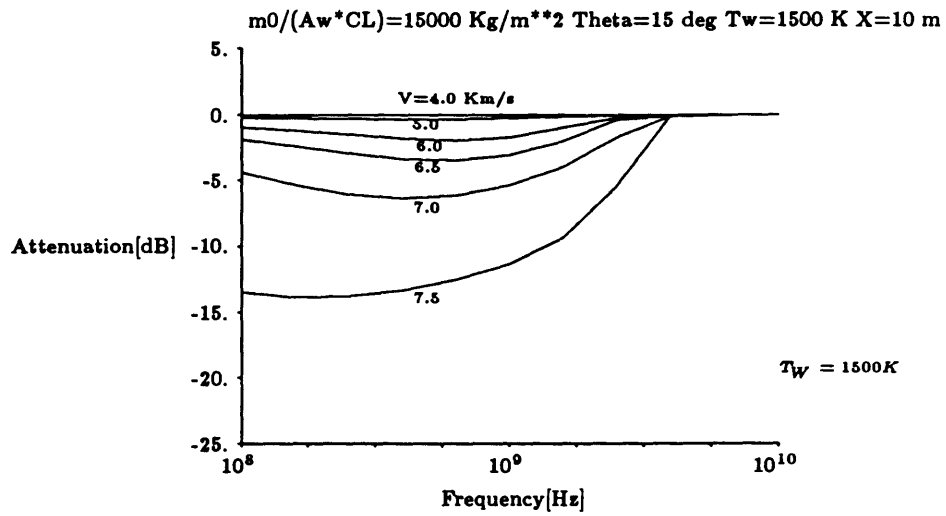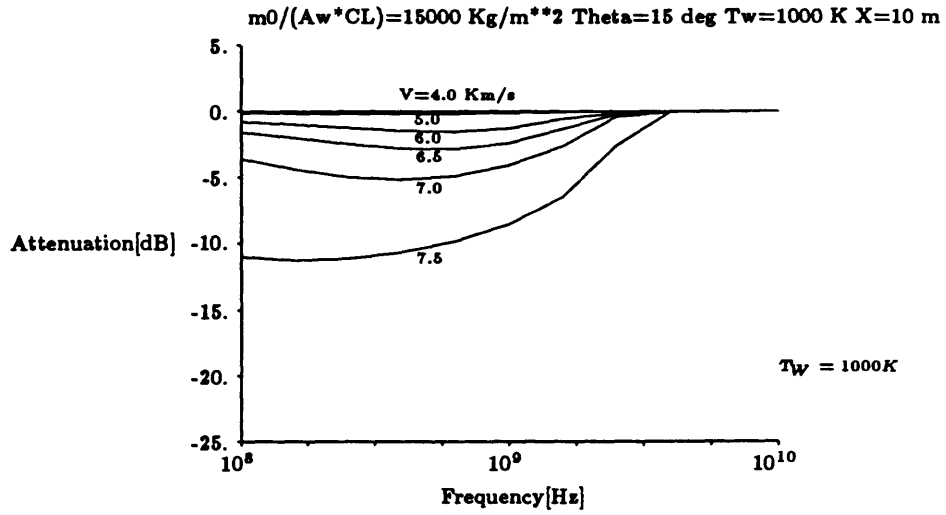
Figure 5.26: Effect of wall temperature on the attenuation of electromagnetic waves
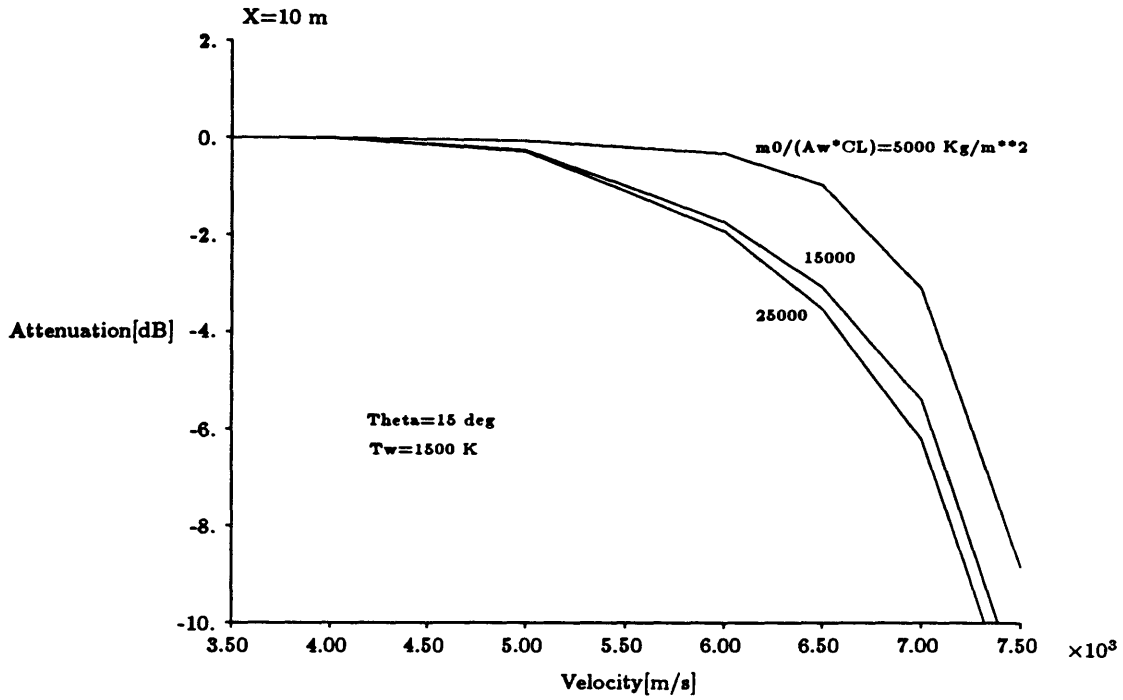
Figure 5.27: Effect of trajectory on the attenuation of electromagnetic waves at 1 GHz
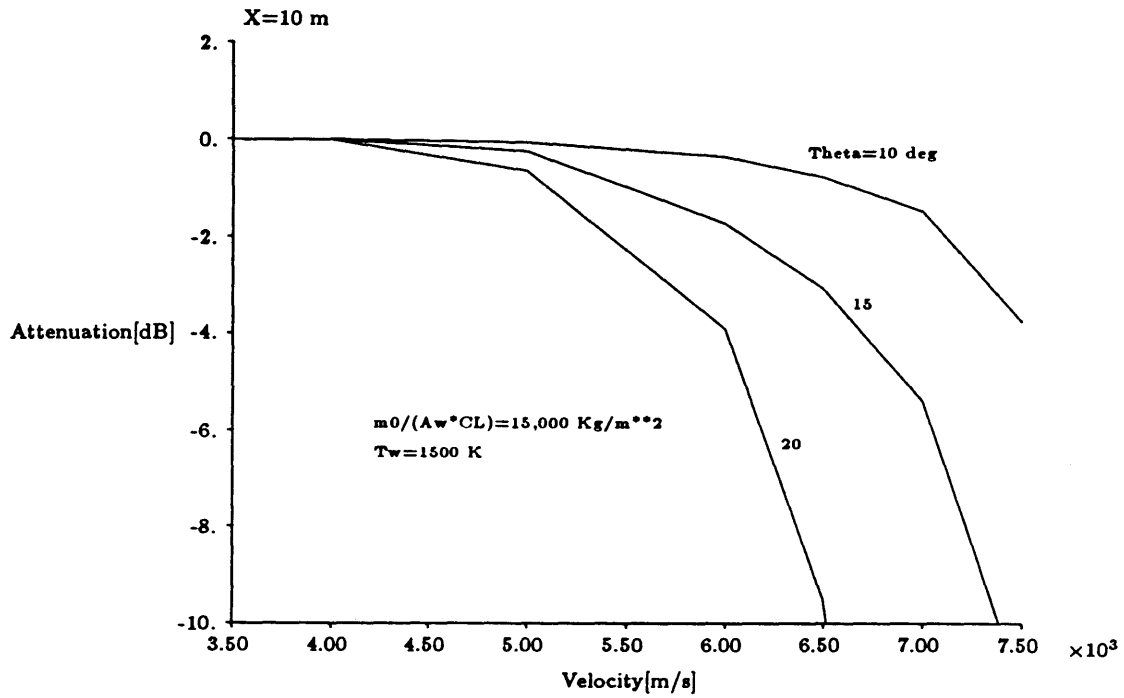
Figure 5.28: Effect of wedge angle on the attenuation of electromagnetic waves at 1 GHz
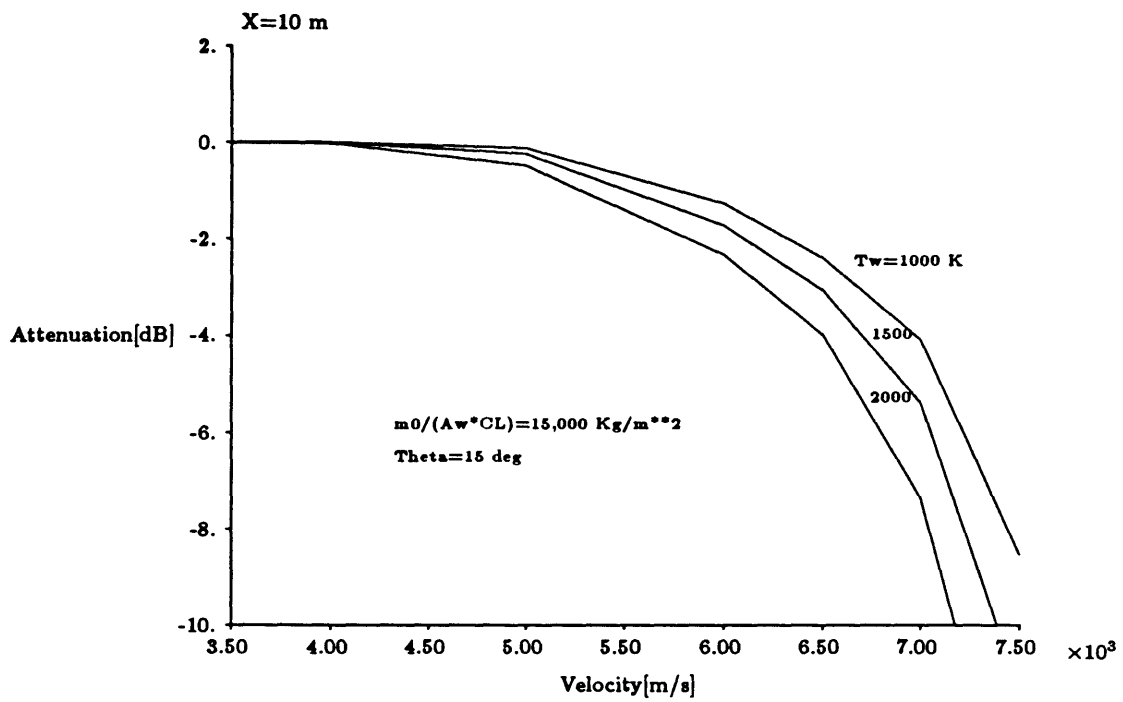
Figure 5.29: Effect of wall temperature on the attenuation of electromagnetic waves at 1 GHz

Chapter 6

Conclusions

Typical SSTO vehicle trajectories have been studied to evaluate the degree of attenuation of the electromagnetic waves propagating to and from the vehicle. The forebody of the vehicle is simulated by a two-dimensional wedge and the high temperature air chemistry associated with the shock and the boundary layer over the wedge is investigated. Electromagnetic waves with various frequencies propagating in the direction normal to the wedge surface are considered to evaluate the attenuation of their power. The general effects of trajectory, velocity, wedge angle, and wall temperature are studied.

In the inviscid flow region behind the shock, the finite rate chemistry is considered. The production of electrons becomes important above V=6.5 Km/s or M=20. The lower trajectory, due to the higher density of the air, gives higher electron density; however, the number density of electrons is still on the order of $10^3 m^{-3}$ approximately 10 m from the shock for $\theta = 15°$ at M=20. The electron density increases significantly with an increase in the wedge angle. For $\theta = 20°$ at M=20, a large number of electrons are produced rapidly right behind the shock and the number density reaches the order of $10^{14} m^{-3}$ a few meters past the shock at M=20.

Based on the experimental results on the transition Reynolds number[8], the boundary layer is assumed to be fully laminar. The chemical composition in equilibrium in the boundary layer are calculated. The boundary layer thickness increases with velocity from about 1 cm at V=3 Km/s (M=10) to about 8 cm at V=7.5 Km/s (M=25) for $\theta = 15°$ and $T_W = 1500K$ along the middle trajectory. The number density of electrons can be considerably large in the boundary layer; it reaches the order of $10^{16}m^{-3}$ above V=5 Km/s (M=16). The lower trajectory gives a thinner boundary layer with a larger maximum electron density. The increase in wedge angle decreases the boundary layer thickness and increases the electron density significantly. The effect of wall temperature is noticeable only in the vicinity of the wall.

The attenuation of electromagnetic waves are estimated along the typical trajectories and the effects of trajectory, wedge angle, and wall temperature are evaluated. The antenna location is selected to be 10 m from the leading edge. The major results are as follows

- The attenuation of electromagnetic waves becomes important above V=5 Km/s (M= 16) below some critical frequency, which is on the order of 1 GHz. Below this critical frequency, the magnitude of attenuation exceeds 3 dB above M=20 and reaches 10 dB at M=25.

- As the altitude of trajectory decreases, the attenuation increases and the critical frequency increases from 2.4 GHz at the upper trajectory to 6.3 GHz at the lower trajectory. A considerable difference in the attenuation is observed between the upper and middle trajectory.

- The increase in wedge angle increases the attenuation significantly and the critical frequency increases from 2.4 GHz for $\theta = 10°$ to 10 GHz for $\theta = 20°$.

- The effect of wall temperature on the attenuation is relatively small for 1000 K $\leq T_W \leq$ 2000 K and the critical frequency increases only slightly from 4 GHz for $T_W = 1000K$ to 6 GHz for $T_W = 2000K$.

The calculations presented here are based on a very simplified flow model over a simple geometry. However, the results of the calculations suggest that it would be difficult to communicate with the SSTO vehicle above M=16 with the radio frequencies below X band.

Bibliography

[1] Bachynski,M.P. and Cloutier,G.G., "Communications In The Presence of Plasma Media," *Dynamics of Manned Lifting Planetary Entry*, John Wiley & Sons, Inc.,1963, pp.206-298.

[2] Huber,P.W. and Sims,T., "Research Approaches To The Problem of Reentry Communications Blackout," *Proceedings of The Third Symposium on The Plasma Sheath -Plasma Electromagnetics of Hypersonic Flight*,Vol.2, Electrical Properties of Shock-Ionized Flow Fields,AFCRL-67-0280,1967,pp.1-34.

[3] Dunn,M.G.,Daiber,J.W.,Lordi,J.A.,and Mates, R. E., "Estimates of Nonequilibrium Ionization Phenomena in The Inviscid APOLLO Plasma Sheath," *Proceedings of The Third Symposium on The Plasma Sheath -Plasma Electromagnetics of Hypersonic Flight*,Vol.2, Electrical Properties of Shock-Ionized Flow Fields,AFCRL-67-0280,1967,pp.35-94.

[4] Martinez-Sanchez,M., "Fundamentals of Hypersonic Airbreathing Propulsion," *AIAA Professional Study Series*, July 9-10,1988.

[5] *U.S. Standard Atmosphere 1962*, NASA, USAF,and U.S.Weather Bureau, Washington,D.C., December 1962.

[6] Bussing,Thomas, and Eberhardt,Scott., "Chemistry Associated with Hypersonic Vehicles," AIAA Paper no.87-1292.

[7] Gnoffo,P. A., Gupta, R. N., and Shinn,J. L., "Conservation Equations and Physical Models for Hypersonic Air Flows in Thermal and Chemical Nonequilibrium," NASA TP 2867, 1989.

[8] Stetson,Kenneth,F., "On Predicting Hypersonic Boundary Layer Transition," AFWAL-TM-84-160-FIMG. Flight Dynamics Laboratory, Air Force Wright Aeronautical Laboratories, Wright-Patterson Air Force Base, Ohio,March 1987.

[9] Anderson,J. D., "Hypersonic and High Temperature Gas Dynamics," McGraw-Hill,1989.

[10] Dorrance,W.H., "Viscous Hypersonic Flow," McGraw-Hill,New York,1962.

[11] Hansen,C.F., "Approximations for the Thermodynamic and Transport Properties of High-Temperature Air," NASA TR R-50, 1959.

[12] Press,W.H.,Flannery,B.P.,Teukolsky,S. A.,Vetterling,W. T., "Numerical Recipes," Cambridge University Press,1986.

[13] Ginzburg,V.,L., "The Propagation of Electromagnetic Waves in Plasmas," Pergamon Press,1970.

[14] Dunn,M.G.,and Kang,S.W., "Theoretical and Experimental Studies of Reentry Plasmas," NASA CR-2232, April,1973.

[15] Cruise,D.R., "Notes on the Rapid Computation of Chemical Equilibria," *The Journal of Physical Chemistry*, Vol.68,1964,pp.3797-3802.

[16] McBride,B.J.,Heimel,S.,Ehlers,J.G., and Gordon,S., "Thermodynamic Properties to 6000° K for 210 Substances involving the First 18 Elements," NASA SP-3001,1963.

[17] Esch,D.D.,Siripong,A. and Pike, R. W., "Thermodynamic Properties in Polynomial Form for Carbon, Hydrogen,Nitrogen,and Oxygen Systems from 300 to 15000° K," NASA-RFL-TR-70-3,1971.

[18] Wakelyn,N.T. and McLain,Allen G., "Polynomial Coefficients of Thermochemical Data for the C-H-O-N System," NASA-TM-X-72657,1975.

[19] Allis,W.P., "Electrons,Ions,and Waves," The M.I.T. Press, Cambridge,1967.

Appendix A

Reaction Model of High
Temperature Air

This appendix contains the reaction model of high temperature air and the constants used in the expressions for the forward and backward rate constants given by Eqs.(3.21) and (3.22). These data were compiled by Dunn and Kang in Ref. [14] and the table is found in Ref.[7]. The units of k_f^r and k_b^r are expressed in $cm^3, g \cdot mol$, and seconds, in the combination appropriate for the given chemical equation.

Table A.1:Reaction model of Dunn and Kang(1/2)

r	Reaction	C_f^r	n_f^r	E_f^r/k	C_b^r	n_b^r	E_b^r/k
1	$O_2 + M \leftrightarrow 2O + M (M = N, NO)$	3.600E+18	-1.00	5.950E+04	3.000E+15	-0.50	0.0
2	$O_2 + O \leftrightarrow 2O + O$	9.000E+19	-1.00	5.950E+04	7.500E+16	-0.50	0.0
3	$O_2 + O_2 \leftrightarrow 2O + O_2$	3.240E+19	-1.00	5.950E+04	2.700E+16	-0.50	0.0
4	$O_2 + N_2 \leftrightarrow 2O + N_2$	7.200E+18	-1.00	5.950E+04	6.000E+15	-0.50	0.0
5	$N_2 + M \leftrightarrow 2N + M (M = O, NO, O_2)$	1.900E+17	-0.50	1.130E+05	1.100E+16	-0.50	0.0
6	$N_2 + N \leftrightarrow 2N + N$	4.085E+22	-1.50	1.130E+05	2.270E+21	-1.50	0.0
7	$N_2 + N_2 \leftrightarrow 2N + N_2$	4.700E+17	-0.50	1.130E+05	2.720E+16	-0.50	0.0
8	$NO + M \leftrightarrow N + O + M (M = O_2, N_2)$	3.900E+20	-1.50	7.550E+04	1.000E+20	-1.50	0.0
9	$NO + M \leftrightarrow N + O + M (M = O, N, NO)$	7.800E+20	-1.50	7.550E+04	2.000E+20	-1.50	0.0
10	$NO + O \leftrightarrow O_2 + N$	3.200E+09	1.00	1.970E+04	1.300E+10	1.00	3.580E+03
11	$N_2 + O \leftrightarrow NO + N$	7.000E+13	0.00	3.800E+04	1.560E+13	0.00	0.0
12	$O_2^+ + O \leftrightarrow O_2 + O^+$	2.920E+18	-1.11	2.800E+04	7.800E+11	0.50	0.0
13	$N_2 + N^+ \leftrightarrow N_2^+ + N$	2.020E+11	0.81	1.300E+04	7.800E+11	0.50	0.0
14	$NO^+ + O \leftrightarrow NO + O^+$	3.630E+15	-0.60	5.080E+04	1.500E+13	0.0	0.0
15	$N_2 + O^+ \leftrightarrow N_2^+ + O$	3.400E+19	-2.00	2.300E+04	2.480E+19	-2.20	0.0
16	$NO^+ + O_2 \leftrightarrow NO + O_2^+$	1.800E+15	0.17	3.300E+04	1.800E+13	0.50	0.0
17	$NO^+ + N \leftrightarrow NO + N^+$	1.000E+19	-0.93	6.100E+04	4.800E+14	0.00	0.0

e A.1:Reaction model of Dunn and Kang (2/2)

Reaction	C_f^r	n_f^r	E_f^r/k	C_b^r	n_b^r	E_b^r/k
$N + O \leftrightarrow NO^+ + e^-$	1.400E+06	1.50	3.190E+04	6.700E+21	-1.50	0.0
$O + O \leftrightarrow O_2^+ + e^-$	1.600E+17	-0.98	8.080E+04	8.000E+21	-1.50	0.0
$N + N \leftrightarrow N_2^+ + e^-$	1.400E+13	0.00	6.780E+04	1.500E+22	-1.50	0.0
$O + e^- \leftrightarrow O^+ + e^- + e^-$	3.600E+31	-2.91	1.580E+05	2.200E+40	-4.50	0.0
$N + e^- \leftrightarrow N^+ + e^- + e^-$	1.100E+32	-3.14	1.690E+05	2.200E+40	-4.50	0.0
$O_2 + N_2 \leftrightarrow NO + NO^+ + e^-$	1.380E+20	-1.84	1.410E+05	1.000E+24	-2.50	0.0
$N_2 + NO \leftrightarrow N_2 + NO^+ + e^-$	2.200E+15	-0.35	1.080E+05	2.200E+26	-2.50	0.0
$NO^+ + O \leftrightarrow O_2 + N^+$	1.340E+13	0.31	7.727E+04	1.000E+14	0.00	0.0
$O_2 + NO \leftrightarrow NO^+ + O_2 + e^-$	8.800E+16	-0.35	1.080E+05	8.800E+26	-2.50	0.0

Appendix B

Calculation of Equilibrium Composition

This appendix describes a method to compute the chemical composition in equilibrium following the approach presented by Cruise[15].

First, the "optimized basis" is chosen. The optimized basis is a set of molecular species which satisfies the following conditions:

- It contains the chemical elements from which all other species can be formed by chemical reactions.

- The components A_j ($j = 1, S$) are chosen so that the corresponding molar amounts n_j are as large as possible.

The chemical reaction which forms the ith species A_i from the basis is written as

$$A_i = \sum_{j=1}^{S} \nu_{ij} A_j \tag{B.1}$$

where ν_{ij} is the stoichiometric mole number matrix. A stoichiometric change $\Delta\xi$ in n_i causes the following changes in the composition

$$n_i' = n_i + \Delta\xi \tag{B.2}$$

$$n_j' = n_j - \nu_{i,j}\Delta\xi \qquad 1 \le j \le S \tag{B.3}$$

and the primed n_i denotes the molar amounts after the change.

The equilibrium constant K_i is written as

$$K_i = \prod_j p_j^{\nu_{ij}} p_i^{-1} \tag{B.4}$$

Then

$$\sum_{j=1}^{S} \nu_{ij} \ln(\frac{n_j}{\sum_i n_i} p) - \ln(\frac{n_i}{\sum_i n_i} p) = \ln K_i \tag{B.5}$$

On the other hand, K_i is given by

$$\ln K_i = \frac{1}{\Re T}[g_i - \sum_{j=1}^{S} \nu_{ij} g_j] \tag{B.6}$$

where g_i is the standard Gibbs free energy of the ith species at P=1 atm, which is a function of only T. The thermodynamic data in functional form are available in the literature such as [16,17,18]. Thus, if T is given, K_i is uniquely determined.

If the current molar guesses for n_i are not correct, the left-hand-side of Eq.(B.5) will be some value, denoted $\ln Q_i$ other than $\ln K_i$. The iteration procedure is done until the value of Q_i approaches that of K_i within a certain tolerance. The correction $\Delta \xi$ for the difference between $\ln K_i$ and $\ln Q_i$ is evaluated by differencing Eq.(B.5) with respect to ξ

$$(-\sum_{j=1}^{S} \frac{\nu_{ij}^2}{n_j} - \frac{1}{n_i}) d\xi = d(\ln K_i) \tag{B.7}$$

where $p/\sum_i n_i$ is assumed to be constant. Then the stoichiometric correction for species i is obtained by applying Newton's method

$$\Delta \xi = (\ln K_i - \ln Q_i)/(-\sum_{j=1}^{S} \frac{\nu_{ij}^2}{n_j} - \frac{1}{n_i}) \tag{B.8}$$

The new n_i and n_j are obtained from Eqs.(B.2) and (B.3), which do not alter the gram-atom amount of any chemical element. Therefore the initial guesses for n_i do not need to be close to the correct values, but must be chosen so that the gram-atom amount of each chemical element is correct. The correction is repeated until $|\ln K_i - \ln Q_i|$ becomes within a specified tolerance.

69

Appendix C

Effective Collision Frequency

This appendix derives the expression for the effective collision frequency, which is used in this thesis, based on Ref. [13].

When the distribution function $f(\vec{r}, \vec{v}, t)$ is nearly isotropic, it is convenient to expand the distribution function in spherical harmonics in velocity space

$$f(\vec{r}, \vec{v}, t) = f_{00} + \frac{\vec{v} \cdot \vec{f_1}(v)}{v} + \cdots \tag{C.1}$$

where

$$f_{00} = n \left(\frac{m}{2\pi\kappa T} \right)^{\frac{3}{2}} e^{-\frac{mv^2}{2\kappa T}} \tag{C.2}$$

Then Boltzmann's equation become [19]

$$\frac{\partial \vec{f_1}}{\partial t} + \frac{e\vec{E}}{m} \frac{\partial f_{00}}{\partial v} + \nu(v)\vec{f_1} = 0 \tag{C.3}$$

where $\nu(v)$ is the collision frequency. $\vec{f_1}$ has a solution of the form:

$$\vec{f_1} = -\frac{e\vec{E}\partial f_{00}/\partial v}{m[i\omega + \nu(v)]} \tag{C.4}$$

The total current density is

$$
\begin{aligned}
\vec{J} &= e \int \vec{v} f \, d\vec{v} \\
&= e \int \vec{v} \frac{\vec{v} \cdot \vec{f_1}}{v} d\vec{v} \\
&= e \int \vec{v}(\vec{v} \cdot \vec{f_1}) v \, dv \, d\Omega \\
&= \frac{4\pi e}{3} \int_0^\infty \vec{f_1} v^3 \, dv
\end{aligned}
$$

$$= \frac{8e^2 n \vec{E}}{3\sqrt{\pi}m} \int_0^\infty \frac{u^4 e^{-u^2} du}{i\omega + \nu(v)}$$

$$= \frac{8e^2 n \vec{E}}{3\sqrt{\pi}m} \left\{ \int_0^\infty \frac{\nu(u) u^4 e^{-u^2} du}{\omega^2 + \nu^2(u)} - i\omega \int_0^\infty \frac{u^4 e^{-u^2} du}{\omega^2 + \nu^2(u)} \right\} \tag{C.5}$$

where the spherical polar coordinates in velocity space with the polar axis along $\vec{f_1}$ have been used so that

$$d\vec{v} = v^2 dv d\Omega = 2\pi v^2 \sin\theta dv d\theta \tag{C.6}$$

and θ is the angle between $\vec{f_1}$ and $\vec{v}$. The following relations are also used

$$u = \left(\frac{m}{2\kappa T} \right)^{\frac{1}{2}} v \tag{C.7}$$

$$\frac{\partial f_{00}}{\partial v} = -\frac{mv f_{00}}{\kappa T}$$

$$= -\left(\frac{n}{2\pi^{3/2}} \right) \left(\frac{m}{\kappa T} \right)^2 u e^{-u^2} \tag{C.8}$$

Since the total current density $\vec{J'}$ can be written as

$$\vec{J'} = \sigma \vec{E} \tag{C.9}$$

where

$$\sigma = \frac{ne^2 \nu_{eff}}{m(\omega^2 + \nu_{eff}^2)} - i\omega \frac{ne^2}{m(\omega^2 + \nu_{eff}^2)} \tag{C.10}$$

Comparing Eq.(C.5) and Eq.(C.9) with Eq.(C.10), we have

$$\frac{\nu_{eff}}{\omega^2 + \nu_{eff}^2} = \frac{8}{3\sqrt{\pi}} \int_0^\infty \frac{\nu(u) u^4 e^{-u^2} du}{\omega^2 + \nu^2(u)} \tag{C.11}$$

For the special case $\omega^2 \gg \nu_{eff}^2$

$$\nu_{eff} = \frac{8}{3\sqrt{\pi}} \int_0^\infty \nu u^4 e^{-u^2} du \tag{C.12}$$

$$= \frac{2}{3\sqrt{2\pi}} \left(\frac{m}{\kappa T} \right)^{\frac{5}{2}} \int_0^\infty \nu v^4 e^{-\frac{mv^2}{2\kappa T}} dv \tag{C.13}$$

- For collisions with molecules

Regarding the molecule as a hard sphere of radius a, ν_m is written as

$$\nu_m = \pi a^2 v n_m \tag{C.14}$$

71

Substituting Eq.(C.14) in Eq.(C.13), the effective collision frequency with molecules is obtained as

$$\nu_{eff} = \frac{4\pi}{3}a^2\bar{v}n_m \tag{C.15}$$

$$\bar{v} = \left(\frac{8\kappa T}{\pi m}\right)^{\frac{1}{2}} \tag{C.16}$$

Although this result is obtained assuming that $\omega^2 \gg \nu_{eff}^2$, the effect of the frequency ω is not significant for the wide range of ω[13].

- For collisions with ions

  The cross section is given by Rutherford's formula:

$$\nu_i = q_i(v)vn_i \tag{C.17}$$

$$q_i(v) = 2\pi\left(\frac{e^2}{mv^2}\right)^2 \ln(1 + \cot^2\frac{1}{2}\theta_{min})$$

$$= 2\pi\left(\frac{e^2}{mv^2}\right)^2 \ln(1 + p_m^2 m^2 v^4/e^4) \tag{C.18}$$

where θ_{min} is the minimum angle of deflection and $p_m = \left(\frac{e^2}{mv^2}\right)\cot\frac{1}{2}\theta_{min}$ is the maximum impact parameter. Substituting Eq.(C.17) in Eq.(C.13) with $p_m = \left(\frac{\kappa T}{8\pi e^2 n_i}\right)^{\frac{1}{2}}$, the expression for the effective collision frequency with ions is obtained[13] as

$$\nu_{eff,i} = \pi\frac{e^4}{(\kappa T)^2}\bar{v}n_i \ln\left(0.37\frac{\kappa T}{e^2 n_i^{1/3}}\right) \tag{C.19}$$

where *the cgs system* has been used.

Appendix D

Thermodynamic Data in Polynomial Form

This appendix contains the necessary constants for the calculation of enthalpy H, Gibbs free energy G, specific heat at constant pressure c_p, and entropy S by the following polynomial forms:

$$\frac{c_p^0}{\Re} = A_1 + A_2 T + A_3 T^2 + A_4 T^3 + A_5 T^4 \tag{D.1}$$

$$\frac{H_T^0}{\Re T} = A_1 + \frac{A_2}{2}T + \frac{A_3}{3}T^2 + \frac{A_4}{4}T^3 + \frac{A_5}{5}T^4 + \frac{A_6}{T} \tag{D.2}$$

$$\frac{G_T^0}{\Re T} = A_1(1 - \ln T) - \frac{A_2}{2}T - \frac{A_3}{6}T^2 - \frac{A_4}{12}T^3 - \frac{A_5}{20}T^4 + \frac{A_6}{T} - A_7 \tag{D.3}$$

$$\frac{S_T^0}{\Re} = A_1 \ln T + A_2 T + \frac{A_3}{2}T^2 + \frac{A_4}{3}T^3 + \frac{A_5}{4}T^4 + A_7 \tag{D.4}$$

where $\Re$ is the universal gas constant and the superscript $(^0)$ denotes the quantity at standard state:the pure component at 1 atmosphere pressure. The elements at 298° K and one atmosphere pressure are selected for the reference state. The constants, A_1 through A_7, are found in Refs. [16,17,18] and shown in Table D.1.

Table D.1:Polynomial coefficients for thermodynamic data in equilibrium(1/3): for each species, the first set of coefficients is for 300 K $\leq$ T $\leq$ 1000 K, the second set is for 1000 K $\leq$ T $\leq$ 5000 K, the third set is for 1000 K $\leq$ T $\leq$ 6000 K, and the fourth set is for 6000 K $\leq$ T $\leq$ 15000 K.

species	A_1	A_2	A_3	A_4	A_5	A_6	A_7
N2	3.6916148	-1.3332552E-3	2.6503100E-6	-9.7688341E-10	-9.9772234E-14	-1.0628336E3	2.2874980
	2.8545761	1.5976316E-3	-6.2566254E-7	1.1315849E-10	-7.6897070E-15	-8.9017445E2	6.3902879
	3.221	9.878E-4	-2.907E-7	3.938E-11	-2.000E-15	-1.043E3	4.326
	3.727	4.684E-4	-1.140E-7	1.154E-11	-3.293E-16	-1.043E3	1.294
O2	3.7189946	-2.5167288E-3	8.5837353E-6	-8.2998716E-9	2.7082180E-12	-1.0576706E3	3.9080704
	3.5976129	7.8145603E-4	-2.2386670E-7	4.2490159E-11	-3.3460204E-15	-1.1927918E3	3.7492659
	3.316	1.151E-3	-3.726E-7	6.186E-11	-3.666E-15	-1.044E3	5.393
	3.721	4.254E-4	-2.835E-8	6.050E-13	-5.186E-18	-1.044E3	3.254
N	2.5147937	-1.1243791E-4	2.9647506E-7	-3.2464049E-10	1.2595465E-13	5.6127767E4	4.1193032
	2.4422261	1.2276187E-4	-8.4992719E-8	2.1400830E-11	-1.2511058E-15	5.6148821E4	4.4925708
	2.474	9.097E-5	-7.814E-8	2.218E-11	-1.489E-15	5.609E4	4.300
	2.746	-3.909E-4	1.338E-7	-1.191E-11	3.369E-16	5.609E4	2.872
O	3.0218894	-2.1737249E-3	3.7542203E-6	-2.9947200E-9	9.0777547E-13	2.9137190E4	2.6460076
	2.5372567	-1.8422190E-5	-8.8017921E-9	5.9643621E-12	-5.5743608E-16	2.9230007E4	4.9467942
	2.670	-1.970E-4	7.193E-8	-8.901E-12	4.002E-16	2.915E4	4.504
	2.548	-5.952E-5	2.701E-8	-2.798E-12	9.380E-17	2.915E4	5.049

Table D.1: Polynomial coefficients for thermodynamic data in equilibrium(2/3): for each species, the first set of coefficients is for 300 K $\leq$ T $\leq$ 1000 K, the second set is for 1000 K $\leq$ T $\leq$ 5000 K, the third set is for 1000 K $\leq$ T $\leq$ 6000 K, and the fourth set is for 6000 K $\leq$ T $\leq$ 15000 K.

species	A_1	A_2	A_3	A_4	A_5	A_6	A_7
NO	4.1469476	-4.1197237E-3	9.6922467E-6	-7.8633639E-9	2.2309512E-12	9.7447894E3	2.5694290
	3.1529360	1.4059955E-3	-5.7078462E-7	1.0628209E-10	-7.3720783E-15	9.8522048E3	6.9446465
	3.221	1.221E-3	-4.297E-7	6.559E-11	-3.451E-15	9.764E3	6.610
	3.845	2.521E-4	-2.658E-8	2.162E-12	-6.381E-17	9.764E3	3.212
NO+	3.14570870	9.55519742E-4	4.94798549E-8	-5.82257176E-10	3.71322532E-13	1.18114163E5	5.61325399
	3.09453628	1.16390462E-3	-3.68121074E-7	5.21412009E-11	-2.68737891E-15	1.18116546E5	5.84919244
	3.200	1.029E-3	-3.075E-7	4.028E-11	-1.814E-15	1.184E5	5.225
	3.561	6.028E-4	-1.540E-7	1.697E-11	-5.296E-16	1.184E5	3.170
e	1.66876530	5.09538278E-3	-1.20629758E-5	1.26590984E-8	-4.86677487E-12	-6.40159685E2	-8.05830942
	2.37626905	2.07741476E-4	-1.13104855E-7	2.43930105E-11	-1.80291089E-15	-7.01451155E2	-1.10375409E1
	2.500	3.440E-7	-1.954E-10	3.937E-14	-2.573E-18	-7.450E2	-1.173E1
	2.508	-6.332E-6	1.364E-9	-1.094E-13	2.934E-18	-7.450E2	-1.208E1
N2+	3.04870303	1.66691862E-3	-1.69948507E-6	1.22924435E-9	-3.00574994E-13	1.78959920E5	5.21345604
	3.09476368	1.17122886E-3	-3.70803092E-7	5.22559219E-11	-2.63943973E-15	1.78953470E5	5.04447470
	3.397	4.525E-4	1.272E-7	-3.879E-11	2.459E-15	1.826E5	4.205
	3.370	8.629E-4	-1.276E-7	8.087E-12	-1.880E-16	1.826E5	4.073

Table D.1: Polynomial coefficients for thermodynamic data in equilibrium(3/3): for each species, the first set of coefficients is for 300 K $\leq$ T $\leq$ 1000 K, the second set is for 1000 K $\leq$ T $\leq$ 5000 K, the third set is for 1000 K $\leq$ T $\leq$ 6000 K, and the fourth set is for 6000 K $\leq$ T $\leq$ 15000 K.

species	A_1	A_2	A_3	A_4	A_5	A_6	A_7
O2+	3.12931650	2.33851052E-3	-3.76502512E-6	4.08884445E-9	-1.69303299E-12	1.43998062E5	6.21557675
	3.25680775	1.24798926E-3	-4.28714608E-7	7.79714406E-11	-5.44049135E-15	1.43993928E5	5.72232395
	3.243	1.174E-3	-3.900E-7	5.437E-11	-2.392E-15	1.400E5	5.925
	5.169	-8.620E-4	2.041E-7	-1.300E-11	2.494E-16	1.400E5	-5.296
N+	2.29485807	1.42410056E-3	-3.44624981E-6	3.57489851E-9	-1.33750503E-12	2.24104779E5	5.71689741
	2.47957220	8.58290701E-5	-7.51191467E-8	2.11968565E-11	-1.37667111E-15	2.24086690E5	4.94417869
	2.727	-2.820E-4	1.105E-7	-1.551E-11	7.847E-16	2.254E5	3.645
	2.499	-3.725E-6	1.147E-8	-1.102E-12	3.078E-17	2.254E5	4.950
O+	2.56134251	7.07794011E-4	-2.32396110E-6	2.44900956E-9	-8.64456773E-13	1.86385135E5	4.31294272
	2.68420332	-2.47148101E-4	1.10854689E-7	-1.95207915E-11	1.33909023E-15	1.86372113E5	3.80817902
	2.491	2.762E-5	-1.881E-8	3.807E-12	-1.028E-16	1.879E5	4.424
	2.944	-4.108E-4	9.156E-8	-5.848E-12	1.190E-16	1.879E5	1.750